JOURNAL OF GEOPHYSICAL RESEARCH, VOL. 102, NO. C6, PAGES 12,727–12,748, JUNE 15, 1997

Altimeter-derived variability of surface velocities in the California Current System
1. Evaluation of TOPEX altimeter velocity resolution

P. Ted Strub
College of Oceanic and Atmospheric Sciences, Oregon State University, Corvallis, Oregon

Teresa K. Chereskin and Pearn P. Niiler
Scripps Institution of Oceanography, La Jolla, California

Corinne James and Murray D. Levine
College of Oceanic and Atmospheric Sciences, Oregon State University, Corvallis, Oregon

Abstract. In this paper, we evaluate the temporal and horizontal resolution of geostrophic surface velocities calculated from TOPEX satellite altimeter heights. Moored velocities (from vector-averaging current meters and an acoustic Doppler current profiler) at depths below the Ekman layer are used to estimate the temporal evolution and accuracy of altimeter geostrophic surface velocities at a point. Surface temperature gradients from satellite fields are used to determine the altimeter's horizontal resolution of features in the velocity field. The results indicate that the altimeter resolves horizontal scales of 50–80 km in the along-track direction. The rms differences between the altimeter and current meters are 7–8 cm s^{-1}, much of which comes from small-scale variability in the oceanic currents. We estimate the error in the altimeter velocities to have an rms magnitude of 3–5 cm s^{-1} or less. Uncertainties in the eddy momentum fluxes at crossovers are more difficult to evaluate and may be affected by aliasing of fluctuations with frequencies higher than the altimeter's Nyquist frequency of 0.05 cycles d^{-1}, as indicated by spectra from subsampled current meter data. The eddy statistics that are in best agreement are the velocity variances, eddy kinetic energy and the major axis of the variance ellipses. Spatial averaging of the current meter velocities produces greater agreement with all altimeter statistics and increases our confidence that the altimeter's momentum fluxes and the orientation of its variance ellipses (the statistics differing the most with single moorings) represent well the statistics of spatially averaged currents (scales of 50–100 km) in the ocean. Besides evaluating altimeter performance, the study reveals several properties of the circulation in the California Current System: (1) velocity components are not isotropic but are polarized, strongly so at some locations, (2) there are instances of strong and persistent small-scale variability in the velocity, and (3) the energetic region of the California Current is isolated and surrounded by a region of lower energy starting 500–700 km offshore. This suggests that the source of the high eddy energy within 500 km of the coast is the seasonal jet that develops each spring and moves offshore to the central region of the California Current, rather than a deep-ocean eddy field approaching the coast from farther offshore.

1. Introduction

In previous studies, the TOPEX satellite altimeter height data have been verified at their most basic level, in terms of errors in the various range calculations, environmental and orbital height errors [*Fu et al.*, 1994; *Katz et al.*, 1995; *Picaut et al.*, 1995]. Velocities calculated from the altimeter heights have also been evaluated over the equatorial Pacific Ocean by comparisons to current meters [*Menkes et al.*, 1995] and surface drifters [*Yu et al.*, 1995]. In this paper we examine the ability of the TOPEX altimeter to resolve the principal spacescales and timescales of surface velocities (beneath the wind-driven surface Ekman layer) over the midlatitude California Current System. Higher-order velocity statistics (spectra, momentum fluxes, and principal axis ellipses) are also evaluated.

Paper number 97JC00448.
0148-0227/97/97JC-00448$09.00

Ideally, we would like to estimate both the error variance and signal variance spectra, as a function of wavenumber and frequency. In practice, the "ground truth" time series of two-dimensional surface velocity fields necessary to do this are lacking. As an alternative, we evaluate two aspects of the resolution capabilities of geostrophic velocities calculated from the TOPEX height data: (1) the magnitude of the difference between geostrophic currents calculated from TOPEX heights and currents measured by an acoustic Doppler current profiler (ADCP) and conventional current meters below the depth of the wind's influence and (2) the along-track spatial scales of velocity resolved by the sensor.

The accuracy of the altimeter-derived surface velocity statistics and the temporal resolution at a point are addressed by comparison to 13–18 months of velocity measurements at a satellite altimeter crossover point (the location where ascending and descending tracks cross), using measurements from 50–100 m of depth. This gives the most direct estimate of the "errors" in cross-track velocities and momentum fluxes calculated at a point along an altimeter track. We place "errors" in quotes to remind the reader that measured ocean currents include ageostrophic components and small-scale variability that are not resolved by the altimeter's geostrophic velocities, as we discuss further below. The hourly current meter velocity data also allow comparisons of the full variance and covariance ($\overline{u'v'}$) frequency spectra from the measured velocities to those obtained by subsampling the current meters at the 10-day TOPEX sampling period, demonstrating the degree of aliasing due to the TOPEX sampling pattern. The covariance statistics represent momentum fluxes accomplished by eddies in the upper ocean and are an important dynamic quantity which can be calculated only at the crossover points [*Morrow et al.*, 1994], since these are the only locations where both components of horizontal geostrophic velocity can be computed from the along-track altimeter height gradients.

To determine how well the altimeter resolves the spatial scales of velocity variability along the altimeter tracks, we use along-track spatial gradients of sea surface temperature (SST) from the advanced very high resolution radiometer (AVHRR) satellite sensor. In regions where salinities are well correlated with temperatures (or unimportant) and where surface temperatures are representative of deeper temperature features, spatial gradients of SST are related to horizontal velocities through the thermal wind relation. These conditions hold well enough for given times and regions of the California Current to allow a test of the horizontal scales resolved by the altimeter. In the California Current System during late summer and fall, the seasonal jet moves far enough offshore to be seen over large portions of the coarsely spaced altimeter tracks, while still carrying the temperature signal from upwelled water and geostrophic adjustments associated with the meandering jet [*Strub et al.*, 1991]. Thus we use data from fall 1992 and winter 1993 to evaluate the TOPEX altimeter's horizontal resolution. It is important to note that we are not addressing the question of what scales may be well represented in two-dimensional fields constructed from the altimeter data, which involve the use of space-time interpolation. We are addressing the more fundamental question of the horizontal scales of the velocity field that are resolved by the actual measurements along ground tracks.

In the next section we describe the data and methods used in the study. In section 3, the results are presented with respect to the accuracy of the velocity, temporal, and spatial resolution and higher-order velocity statistics. In section 4 we summarize and discuss our conclusions. The Appendix gives details of the geostrophic velocity calculation and the effects caused by changing those details.

2. Data and Methods

2.1. Satellite and In Situ Data

The satellite altimeter data are from cycles 1-111 of the TOPEX geophysical data records (GDRs), obtained from the Jet Propulsion Laboratory (JPL). POSEIDON data are not used. These data cover a period of 3 years (September 1992 to September 1995). Standard environmental corrections are applied [*Callahan*, 1993], including the dry troposphere correction, solid Earth, and pole tides from the GDR. The sea surface height, mean sea surface, dry troposphere, solid earth and pole tides are interpolated to the Zlotnicki-Fu along-track grid with 6.2-km spacing, and the corrections are then subtracted from the sea surface height. The ocean tide is calculated at the grid points and subtracted from the sea surface height using the tide model of *Egbert et al.* [1994]. The resulting signal is the dynamically important variable and is referred to as the "corrected sea surface height." No residual orbit error corrections are removed, since they are expected to be small and to have large spatial scales, producing little effect on the velocities calculated from the along-track gradient of height. Cross-track geostrophic velocities are calculated from the along-track gradient of the height using a centered difference with a span of 62 km (10 grid spacings). Details of the calculation are presented in the Appendix.

The SST gradients come from AVHRR images containing cloud-free regions during periods within several days of the altimeter overpasses. Temperature gradients are calculated from channel 4 alone (11.5 μm), with no multichannel atmospheric correction (since this introduces additional noise into the SST field). A long-term mean is subtracted from the SST data along each track before forming gradients and low-pass filtering the along-track temperature gradients with the same operators used in the geostrophic cross-track velocity calculation (see Appendix). Thus the temperature and height gradients are processed as similarly as possible.

Independent velocity estimates come from five moorings located near the altimeter crossover at 37.1°N, 127.6°W. The mooring array and altimeter crossover are located in water approximately 4800 m in depth, more than 400 km offshore of the continental shelf and slope. Neither bottom topography nor amplified shallow-water tides are a problem at this location.

On the mooring directly under the altimeter crossover, estimates of horizontal velocity are available from a downward looking ADCP mounted in the bridle of a surface buoy. Details of the deployment and processing are given by *Chereskin* [1995]. This record provides approximately a year of overlap with the TOPEX altimeter, from late September

1992 to mid-October 1993. Range gating the signal produces a vertical profile of velocity at 4 m intervals, with the shallowest depth centered at 8 m and the deepest centered at 164 m. The sample rate was 1 Hz for a 5-min interval every 20 min, which reduced velocity aliasing and filter skew bias due to high-frequency surface waves to less than 1 cm s^{-1} in each 5-min ensemble average [*Chereskin et al.*, 1989; *Chereskin and Harding*, 1993; *Chereskin*, 1995].

In addition to the downward looking ADCP, currents are also available from four conventional vector averaging current meters (VACMs) at approximately 100-m depth over periods of 18–24 months. One mooring was located 2.2 km east of the crossover and ADCP mooring, while the other three were located approximately 15 km north, west, and south of the central ADCP mooring. Positions of the moorings relative to the altimeter tracks are shown below. VACM velocities were vector averaged over every 30 min.

Chereskin [1995] used these same ADCP velocities to look at wind-driven Ekman-like currents above 48-m depth. She found most of the wind-driven shear above 48 m, little shear between 48 and 60 m, and somewhat greater geostrophic shear below that. Correlations with the altimeter velocities are also greatest for ADCP velocities between 48 and 60 m and we use the 48-m depth as the best representation of the geostrophic velocities, beneath the wind-driven Ekman layer. Although the 100-m depths of the VACMs are greater than this optimal depth, the mean shear between the 48-m and 100-m ADCP bins is less than 2 cm s^{-1}, and the rms difference between these depths is 5 cm s^{-1}. These measurements from 100-m depth are useful in demonstrating the small-scale variability in the currents that accounts for much of the difference between the altimeter and measured velocities.

2.2. Methods: Accuracy and Temporal Resolution at a Point

The ADCP and altimeter data from the crossover point at 37.10°N, 127.56°W are used to estimate the accuracy of the altimeter's velocity calculation and its temporal resolution at a fixed point. The long-term temporal means of all velocity time series are removed to form velocity "anomalies" for all comparisons reported below. Comparisons of ADCP and altimeter-derived velocities are most directly accomplished by projecting the ADCP velocities onto the cross-track direction of ascending and descending altimeter tracks. Alternatively, estimation of the orthogonal east-west (u) and north-south (v) components of velocity from the two altimeter tracks is possible at the crossover, with additional uncertainty introduced by the fact that the ascending and descending tracks are not orthogonal [*Morrow et al.*, 1994]. The prograde geometry of the TOPEX/POSEIDON orbit has ascending tracks moving from southwest to northeast and descending tracks moving from northwest to southeast, opposite to those from Geosat. Given this geometry, the relationships between the components of the true velocity ($\vec{v} = u\hat{i} + v\hat{j}$) at a crossover and the cross-track velocity of the ascending (V_{ca}) and descending (V_{cd}) tracks are

$$V_{ca} = u\cos\theta - v\sin\theta \tag{1a}$$

$$V_{cd} = u\cos\theta + v\sin\theta \tag{1b}$$

$$u = \frac{V_{ca} + V_{cd}}{2\cos\theta} \tag{1c}$$

$$v = \frac{V_{cd} - V_{ca}}{2\sin\theta} \tag{1d}$$

where θ is the angle between the ground track and the north meridian (symmetric for ascending and descending orbits) and both V_{ca} and V_{cd} are defined positive if they have an eastward component. See Figure 1 of *Mesias and Strub* [1995] for a picture of the geometry.

Assuming the error variances for the cross-track velocities at the crossover are uncorrelated and equal for ascending and descending tracks and are given by σ^2_{vc}, the error variances for the u and v components calculated from (1c) and (1d) at a crossover are (using simple propagation of error)

$$\sigma_u^2 = \frac{\sigma_{vc}^2}{2\cos^2\theta} \approx 0.63\sigma_{vc}^2 \quad \sigma_u = 0.80\sigma_{vc} \tag{2a}$$

$$\sigma_v^2 = \frac{\sigma_{vc}^2}{2\sin^2\theta} \approx 2.36\sigma_{vc}^2 \quad \sigma_v = 1.54\sigma_{vc} \tag{2b}$$

The numerical values on the right are for θ=27.4°, which applies to the TOPEX/POSEIDON orbit at 37.1°N. The point of this calculation is the fact that the expected error variances are different for the two orthogonal components, due to the geometry, and that these change as a function of latitude. Ideally, we would like to first estimate σ_{vc} by finding the rms difference between the cross-track velocity estimated from the altimeter (see (A1)) and the coincident value from the current meters as calculated by (1a) or (1b). This allows estimates of the uncertainties in altimeter-derived u and v values according to (2a) and (2b). Although the time difference between ascending and descending tracks is negligible for the crossover point at 37.1°N, 127.6°W (the ascending track 69 follows the descending track 54 by 14.5 hours), we linearly interpolate the cross-track velocities to a common time before combining them to form the vector velocities.

In comparing the altimeter estimates of geostrophic surface velocity anomalies with the ADCP and VACM subsurface measurements, we need to evaluate several processes in the upper ocean which produce real variability in the currents that geostrophic calculations (altimeter or otherwise) cannot resolve. Geostrophic vertical shears will be created between the surface and the current meters at 48 and 100 m if there are horizontal density gradients in the upper 50–100 m of the water column. Although the meandering jet and eddy system that develops in this region [*Huyer et al.*, 1991; *Paduan and Niiler*, 1990] do include horizontal density gradients, *Kosro et al.* [1991] estimate mixed layer depths to be 60–90 m in winter and 20–60 m in summer. Thus density gradients are weak in the upper 40–60 m of the water column for much of the year.

Another source of unresolved vertical shear is the wind-driven Ekman current in the upper ocean. *Chereskin* [1995] analyzes the "defect" of velocities above 48 m and shows that most of the observed wind-driven velocity occurs above this depth. Any residual wind-driven Ekman flow at 48 m

will be much lower in magnitude than the maximum value of 5 cm s^{-1} that Chereskin found near the surface. Near-inertial motions are another potential source of error, since the surface height signature of these motions will remain in the altimeter heights but will be removed from the ADCP data by the 40-hour filter. *D'Asaro et al.* [1995] report spatially varying inertial currents in the eastern North Pacific with 10 cm s^{-1} horizontal changes over distances of 50 km. We estimate maximum surface slopes associated with these ageostrophic motions to be a change of 1-2 cm over the 50 km distance, equivalent to 2–4 cm s^{-1} in the geostrophic calculation. Finally, internal wave velocities with periods of 5–40 min may be aliased by the burst sampling of the ADCP but will not affect the VACMs. Differences between the spectra of unfiltered velocities from the two sensors indicate that aliasing does occur but contributes less than a few centimeters per second to the unfiltered ADCP data. The 40-hour filter reduces the effects of this aliasing further. Thus we assume that the 48-m velocity is as close to geostrophic as we can expect to find and that ageostrophic velocity components will cause differences of 4 cm s^{-1} or less between the altimeter and filtered ADCP velocities.

2.3. Methods: Horizontal Resolution

To check the horizontal resolution of the altimeter, we estimate the along-track scales of velocity features using the along-track AVHRR temperature gradients and the thermal wind relation. We also use cycle-to-cycle persistence in the horizontal structure of the altimeter's cross-track velocity features to indicate features that are well resolved. The thermal wind relation relates the vertical shear of velocity in one direction to the horizontal gradient of density in a direction perpendicular to the velocity:

$$\frac{\partial V_c}{\partial z} = \frac{g}{\rho f}\frac{\partial \rho}{\partial s} \tag{3a}$$

$$\frac{\partial V_c}{\partial z} = \frac{g}{\rho f}\frac{\partial}{\partial s}\{\rho_o[1 + \alpha(S - S_o) - \beta(T - T_o)]\} \tag{3b}$$

$$\frac{\partial V_c}{\partial z} \approx -\frac{g\beta'}{f}\frac{\partial T}{\partial s} \tag{3c}$$

where z is the vertical dimension, S and T are salinity and temperature, and ρ is the density, represented as a linear function of salinity and temperature around some reference S_o and T_o. The parameter, β, is the coefficient of thermal expansion of salt water and α is the coefficient of expansion due to salinity. The final expression is obtained by assuming that salinity is either insignificant in determining density ($\beta' = \beta$) or is correlated with temperature (β' combines β, α, and the regression coefficient between temperature and salinity). If the value of the velocity is V_c at the surface and goes to zero at some reference depth (level of no motion) Z_r, then $\frac{\partial V_c}{\partial z} \approx V_c/Z_r$ and

$$V_c \approx -\frac{Z_r g\beta'}{f}\frac{\partial T}{\partial s} = -\frac{Z_r g\beta'}{f 2n\Delta s}\Delta T \tag{4}$$

where n is the half span of the centered gradient calculation (we use $2n$ = 10 grid intervals, $2n\Delta s$ = 62 km) and ΔT is the along-track temperature increase over the 62 km.

3. Results

3.1. Regional Circulation Characteristics

Figure 1 shows the horizontal field of SST from an AVHRR image on October 9, 1992 (year day 283), overlain by TOPEX cross-track velocity anomalies from a 7-day period during cycle 2 (year days 279-285). The ADCP data used in this section come from the mooring under the crossing of ascending track 69 and descending track 54. The long-term (1-2 year) means which are removed from the ADCP and VACM data to form velocity anomalies are of order 3–4 cm s^{-1}, whereas daily velocities have magnitudes of up to 30 cm s^{-1}. Thus velocity anomalies and absolute velocities are nearly identical, with an offset equal to approximately 10% of the maximum velocities, and we use the terms velocity and velocity anomaly interchangeably.

This figure and other fields of TOPEX cross-track velocities and AVHRR SST patterns are similar to the summer patterns documented by hydrographic/ADCP surveys during the 1987-1988 coastal transition zone (CTZ) experiment in the same region: a surface jet meanders equatorward on the offshore side of colder water, with less organized flow and SST patterns farther inshore of this jet. Altimeter cross-track velocities alternate in sign on scales of 100–300 km, as the altimeter tracks cross the meandering jet and eddy system. One must remember that only the flow in the direction perpendicular to the altimeter track can be resolved by the geostrophic calculation, except at crossovers. At the crossover at 37.1°N, 127.6°W (the ADCP mooring location), the addition of the two cross-track components produces a velocity anomaly that is directed approximately toward the east at 30 cm s^{-1}.

The equatorward jet on the offshore side of colder water satisfies the thermal wind relation. Surveys from 1987 and 1988 show uplifted isopycnals and isotherms under colder SSTs on the inshore sides of the cyclonic meanders and deepened isotherms under warmer SSTs on the offshore sides of the anticyclonic meanders [*Kosro et al.*, 1991; *Huyer et al.*, 1991]. The correspondence of the deeper thermal structure to the SST patterns is confirmed by *Ramp et al.* [1991], who find significant correlations in the same region between surface and deeper temperatures (down to at least 100-m depth). This correspondence between SST and the deeper thermal structure justifies our use of the thermal wind relation in the upper 100 m of this region of the California Current System.

3.2. Temporal Resolution and Accuracy of the Velocity Statistics

Stick plots of the daily ADCP velocity anomalies from the mooring are presented in Figure 2a, after removing tidal and inertial motions with the low-pass filter (40-hour half power) and the mean velocity from the period (approximately 4 cm s^{-1} to the south). In Figure 2b, the same data are shown subsampled to the TOPEX days, for comparison to the daily ADCP data in Figure 2a and to the TOPEX data in Figure 2c. The TOPEX vectors are reconstructed from the cross-track velocity anomalies using (1c) and (1d). These data qualitatively reveal the temporal aspects of the data, especially the long timescales of the primary modes of variability, consisting of alternating currents with periods

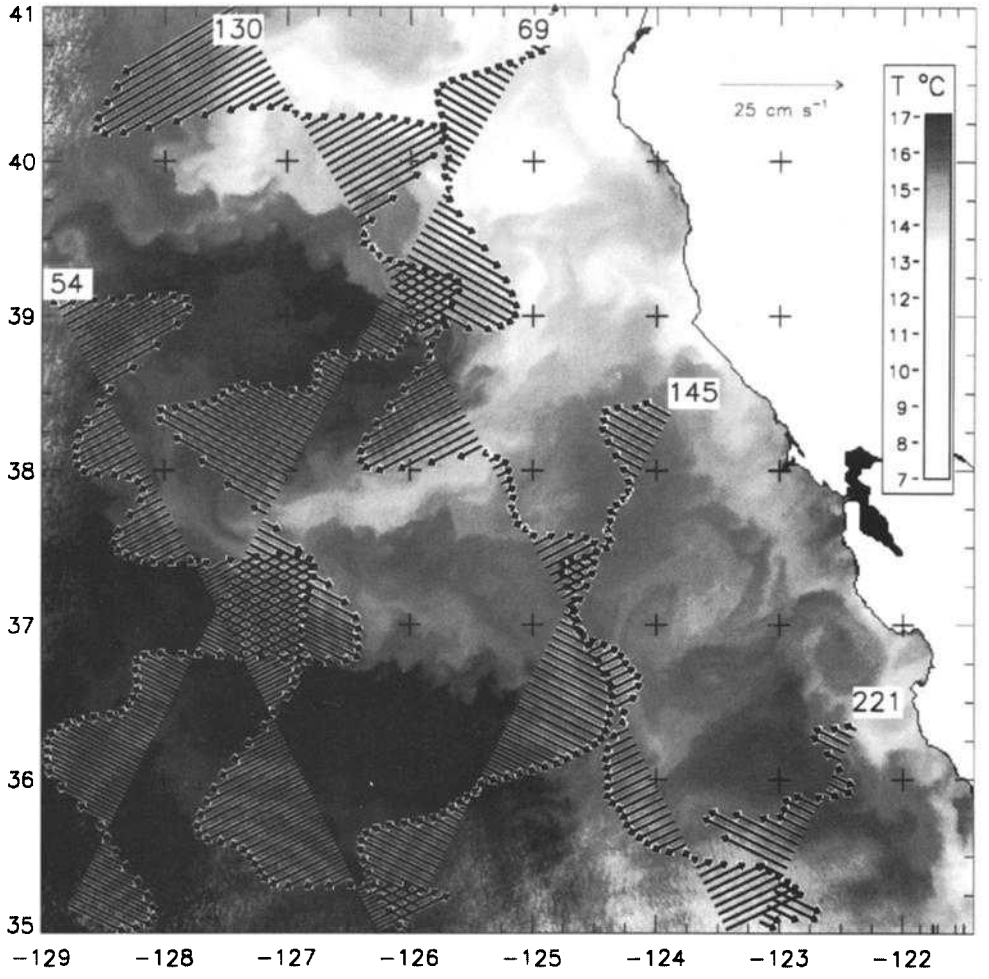

Figure 1. A field of TOPEX cross-track velocities from cycle 2 (October 5–11, 1992), characteristic of late summer and fall, overlain on an SST image from October 9, 1992. Lighter shades denote colder temperatures. The current meter moorings are located under the crossover of tracks 54 and 69.

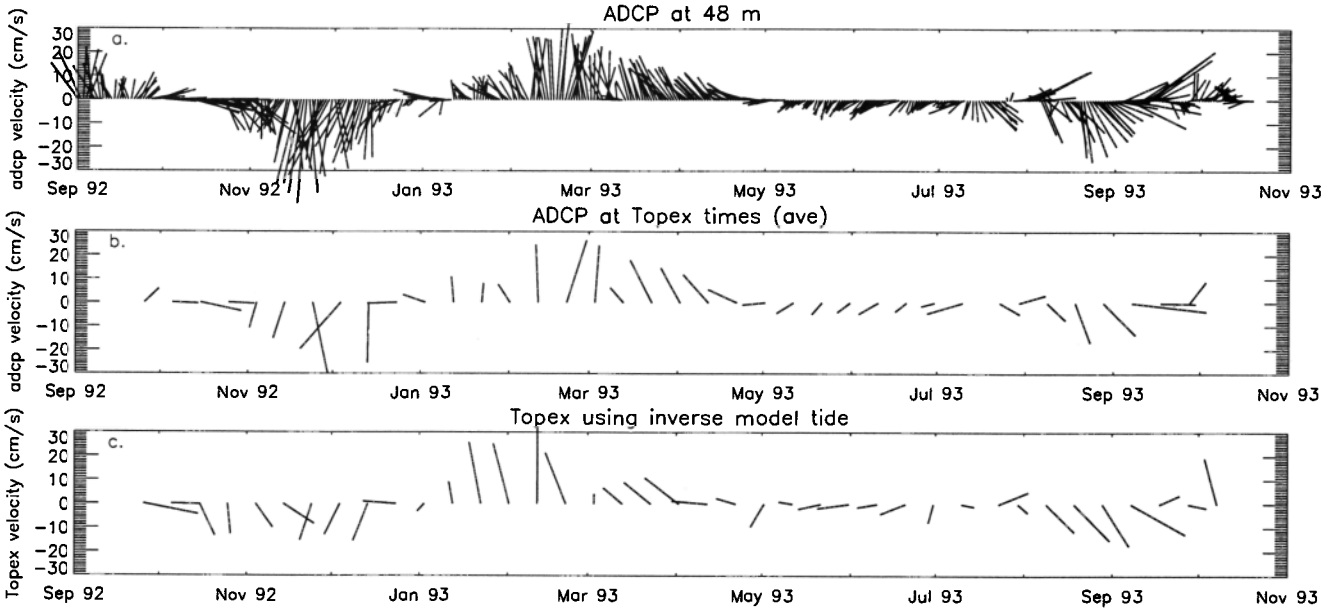

Figure 2. Stick plots of velocity anomalies from the ADCP mooring (48-m bin) and TOPEX crossover at 37.1°N, 127.6°W, from September 1992 through October 1993. (a) Daily low-pass filtered (40-hour half power) ADCP data; (b) 10-day subsampled low-pass ADCP data; (c) TOPEX geostrophic velocities.

of approximately 2–4 months. This long-period variability is associated with the slow movement of the jet meanders and eddy field (Figure 1) past the fixed measurement point. Shorter fluctuations are also apparent in the daily ADCP data. The 10-day subsampling of the ADCP data indicates that the TOPEX sampling is capable of resolving the dominant temporal scales, while missing some of the shorter period variability.

Statistics of the ADCP and TOPEX velocity variability at the mooring/crossover point are presented in Tables 1a and 1b. The components V_{ca} and V_{cd} are the cross-track velocity anomaly components on the ascending (69) and descending (54) altimeter tracks, respectively, while the u and v components are in the normal east and north directions. EKE is eddy kinetic energy and is simply $0.5(\overline{u'^2} + \overline{v'^2})$. The major and minor principal axes and the direction of the major axis (here reported clockwise from north) are calculated following *Morrow et al.* [1994] and *Preisendorfer* [1988]:

$$\sigma_{11} = \frac{1}{2}\{\overline{u'^2} + \overline{v'^2} + [(\overline{u'^2} - \overline{v'^2})^2 + 4(\overline{u'v'})^2]^{\frac{1}{2}}\} \quad (5a)$$

$$\sigma_{22} = (\overline{u'^2} + \overline{v'^2}) - \sigma_{11} \quad (5b)$$

$$\tan\theta' = \frac{\sigma_{11} - \overline{u'^2}}{\overline{u'v'}} \quad (5c)$$

$$\theta = -(\theta' + 90°) \quad (5d)$$

where σ_{11} and σ_{22} are the variances along the major and minor axes, θ' is the direction of the major axis as measured counterclockwise from east, and θ is the direction of the major axis as measured clockwise from north, which we find a more natural orientation.

The variance and covariance statistics in Table 1a show a drop in ADCP variances of approximately 30–40% when the time series are filtered (40-hour half power) to remove tidal and inertial period energy. Subsampling the hourly ADCP data at the TOPEX 10-day period results in only slight changes in the variances but reduces the already low value of eddy momentum flux (covariance, $\overline{u'v'}$) even further. Using monthly means reduces the variances and EKE another 30–40%. Variances of the 10-day TOPEX cross-track velocities are within 20–30% of the ADCP variances for the two tracks, with much smaller (less than 10%) differences in the variances in u and v. Both ADCP and TOPEX data show a moderate polarization in the north-south direction during the common 1-year ADCP period. The magnitude of the TOPEX eddy momentum flux is 40 cm^2 s^{-2} compared to the ADCP value of only 6 cm^2 s^{-2} (both negative). The TOPEX and ADCP principal axis statistics for the same period both show polarization (ratios of 2:1 and 1.5:1 between major and minor axes) but differ in the direction of the major axes by about 20°. The ADCP major axis is nearly due north (7°counterclockwise from north), while the TOPEX major axis about 30°counterclockwise from north (the difference caused mostly by the different magnitudes of the eddy momentum flux). Overall, the eddy momentum flux and the angle show the greatest difference between the TOPEX and 48-m ADCP data.

Table 1a. TOPEX Crossover and 48-m ADCP Statistics: Velocity Variances at the Crossover for Cross-Track Components Along the Ascending (V_{ca}) and Descending (V_{cd}) Track, in the East-West (u) and North-South (v) Directions and Along the Major (σ_{11}) and Minor (σ_{22}) Principal Axes

	σ^2 V_{ca}, cm^2 s^{-2}	σ^2 V_{cd}, cm^2 s^{-2}	σ^2 u, cm^2 s^{-2}	σ^2 v, cm^2 s^{-2}	$\overline{u'v'}$, cm^2 s^{-2}	EKE, cm^2 s^{-2}	Major Axis σ_{11} cm^2 s^{-2}	Minor Axis σ_{22} cm^2 s^{-2}	θ, deg
Raw hourly ADCP, no filter	180	153	149	231	-17	190	235	146	-11
40-hour filter, hourly ADCP	118	94	90	167	-14	128	169	87	-10
40-hour filter, 10-day ADCP-TOPEX times	116	106	101	149	-6	125	150	100	-7
40-hour filter, monthly ADCP	78	71	64	115	-4	89	115	64	-4
10-day TOPEX, ADCP period	142	77	100	144	-40	122	168	77	-31
Monthly TOPEX, ADCP period	115	63	82	114	-32	98	134	62	-32
10-day TOPEX, 3 years	165	125	139	168	-24	153	182	125	-30
Monthly TOPEX, 3 years	119	101	108	118	-11	113	125	101	-33

Covariance ($\overline{u'v'}$), eddy kinetic energy (EKE), and θ, the orientation of the major principal axis, measured clockwise from north, are also shown.

Table 1b. TOPEX Crossover and 48-m ADCP Statistics: RMS Differences in Velocity at the Crossover From Cross-Track and Orthogonal Components

	V_{ca}, cm s^{-1}	V_{cd}, cm s^{-1}	u, cm s^{-1}	v, cm s^{-1}
10-day TOPEX-ADCP rms	7	7	7	8
30-day TOPEX-ADCP rms	3	5	4	5

Statistics computed from the full 3 years of TOPEX data are more energetic than those from the 1-year period (EKE and variances) but have lower covariances. The direction of the TOPEX major axis is stable around -30°over all periods. The degree of polarization of the variance ellipse is more like the ADCP data (ratio of 1.5:1). These differences between statistics calculated over 1 and 3 years indicate that the eddy momentum flux is the most unstable. Because the temporal scales of variability are long (2-4 months), the number of eddies sampled at a single location in a year is small. Even if there is no interannual variability in the eddy field, there are only a few degrees of freedom for records less than 3 or more years.

The rms differences between altimeter and ADCP velocity anomaly components are shown in Table 1b for the data from 10-day cycles and from monthly averages. These indicate a basic difference in cross-track velocities of approximately 7–8 cm s^{-1} for 10-day data, which drops to approximately 3–5 cm s^{-1} for the monthly means. Figure 3 shows scatterplots for each of the 10-day components, 48-m ADCP versus TOPEX, with the values of the correlation between the ADCP and TOPEX components indicated. These correlation values are significant at the 95% level for 5–10 degrees of freedom. Given the long timescales of the dominant velocity fluctuations, the number of degrees of freedom are probably less than 10 for the 1-year record. Figure 2 makes it clear, however, that the altimeter captures this long-period variability. The differences between the ADCP velocities (measured 48 m below the surface at a single point) and the geostrophic cross-track velocities (calculated using a 62-km surface height difference centered on that point) are not only due to errors and noise in the altimeter data. They are also caused by small-scale, horizontal differences in measured point velocities that the geostrophic calculation does not resolve, as well as vertical shears between the surface geostrophic velocities (estimated by the altimeter) and measured velocities at 48 m.

The effects of small-scale vertical and horizontal variability can be evaluated by statistics from the 48- and 100-m ADCP bins and the VACMs from 100-m depth at four moorings surrounding the ADCP mooring, with separations of 15 km. Daily filtered velocity anomalies from two of the moorings are shown in Figures 4a and 4b (located 15 km north and 2 km east of the ADCP mooring), along with the spatially averaged velocity from all four 100-m moorings, decimated to the altimeter's 10-day sampling (Figure 4c) and the 10-day altimeter data (Figure 4d). A horizontal snapshot of velocity anomalies from all five moorings on May 1, 1993, is shown in Figure 4e, along with TOPEX cross-track velocity anomalies from the same time. These show the mooring locations relative to the altimeter tracks and one instance of a persistent small-scale anticyclonic feature, discussed below.

Data from the common 18-month period of VACM mooring data, decimated to the 10-day TOPEX times, are used to calculate the statistics presented in Tables 2a and 2b. Statistics from the 13-month ADCP bins at 48 and 100 m are also presented (the 48-m ADCP statistics are repeated from Table 1a). The rms differences between 48 and 100 m are 5 cm s^{-1}, with a 20–30% decrease in energy with depth, as reflected in lower values of EKE, variances, and principal axis ellipses. The mean shear is less than 2 cm s^{-1} between these depths, partly because some eddies appear to be depth intensified. The eddy momentum flux at 100 m is larger in magnitude than at 48 m and the principal axis ellipse orientation is more counterclockwise (24°versus 7°). The 100-m ADCP velocities are also lower in energy than the central VACM but are more similar to the spatial average of the four VACM currents. Comparing the four VACMs to each other, the energy levels are similar, while the eddy momentum fluxes and principal axis directions can differ by factors of 3–5. Statistics from the western mooring are the most different of the group, with a principal axis orientation more counterclockwise (-34°), similar to the altimeter's orientation of approximately -30°.

An examination of the velocity records in Figure 4a and 4b shows examples of velocities in opposite directions at the northern and central moorings (15 km apart) for periods of several weeks (May 1993). In Figure 4e, the data from all five moorings and the altimeter on May 1 depict an anticyclonic eddy that moved over the array and caused this horizontal variability. The altimeter's cross-track velocities capture the anticyclonic sense and the position of the feature but fail to represent the small-scale nature of the feature and the true velocity at the crossover.

By averaging the velocities from the four moorings for each hour, an estimate of a spatially averaged velocity can be formed over a region approximately 30 km across. Although this spatial averaging is over a smaller region than the 60–80 km smoothing inherent in the altimeter velocity calculation, it is more like the altimeter estimate than currents from the individual moorings. The averaging causes a drop of 17% in EKE for the spatially averaged velocities, as compared with the central mooring (Table 2a), with a greater reduction in $\overline{u'^2}$ (25%) than $\overline{v'^2}$ (13%). The value of the spatially averaged eddy momentum flux is -34 cm^2 s^{-2} for this 18-month period, more like the altimeter's value of -36 cm^2 s^{-2} for the same period, rather than the 48 and

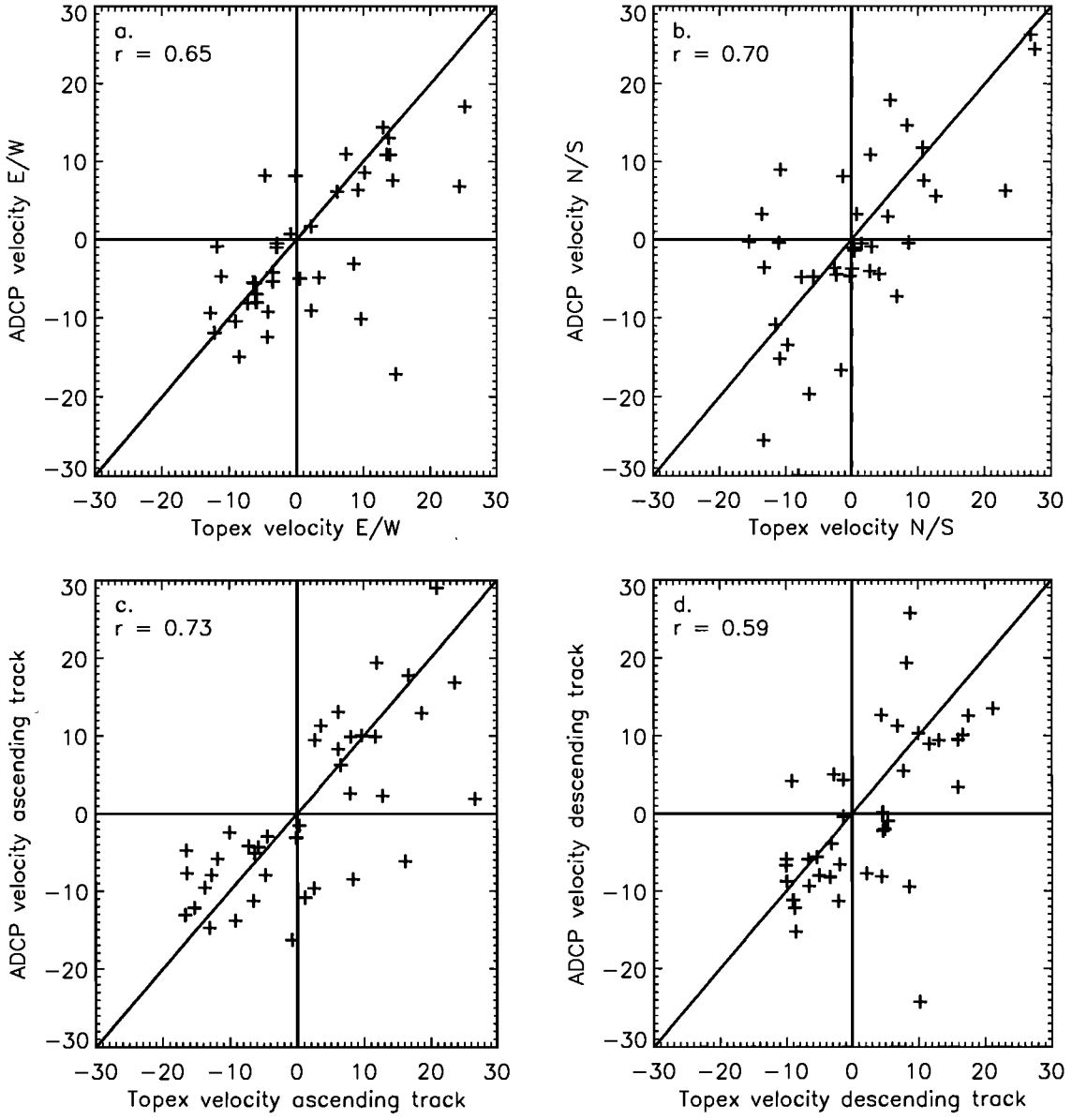

Figure 3. Scatterplots of ADCP versus TOPEX velocity components for the 13 months of data: (a) u, (b) v, (c) V_{ca}, (d) V_{cd}. Units are in centimeters per second. Correlations are shown in the upper left for the data in each panel.

100-m ADCP values of -6 and -17 cm^2 s^{-2} for the 1-year period (the altimeter's value changes very little between the 1-year and 18-month period). This provides evidence that the TOPEX velocities are more representative of spatially averaged currents, eliminating small-scale variability.

The rms differences between TOPEX velocity anomalies and those from the individual 100-m central and southern mooring velocities are 7–8 cm s^{-1} (Table 2b), similar to the difference between TOPEX and ADCP (48 and 100 m) velocity anomalies. Velocities from the northern and western mooring produce slightly higher values. The rms differences between the velocity anomaly components from the central mooring and the surrounding moorings, separated by 15 km, are 5–7 cm s^{-1} (Table 2c), revealing that the degree of small-scale variability in the oceanic velocity field at this location is nearly as large as the rms difference between the TOPEX and ADCP velocities. On the smallest scales, the rms difference between the 100-m ADCP bin and the central VACM (separated by 2 km) is 3–4 cm s^{-1}. We take this to be the level of measured velocity "noise", caused by aliasing of internal waves by the ADCP's burst sampling, very small-scale currents, etc.

As a result of these comparisons, we attribute the 7–8 cm s^{-1} rms differences between the altimeter and the ADCP velocities (at both 48 and 100 m) to contributions of 5–7 cm s^{-1} rms from natural, small-scale, horizontal variability, 5 cm s^{-1} from vertical shears, and 3–4 cm s^{-1} from other unresolved sources and current meter noise. This apportioning accounts for the complete magnitude of the difference between the altimeter and current measurements and suggests that the altimeter error is no greater than the 3–4 cm s^{-1} difference between current meters separated by

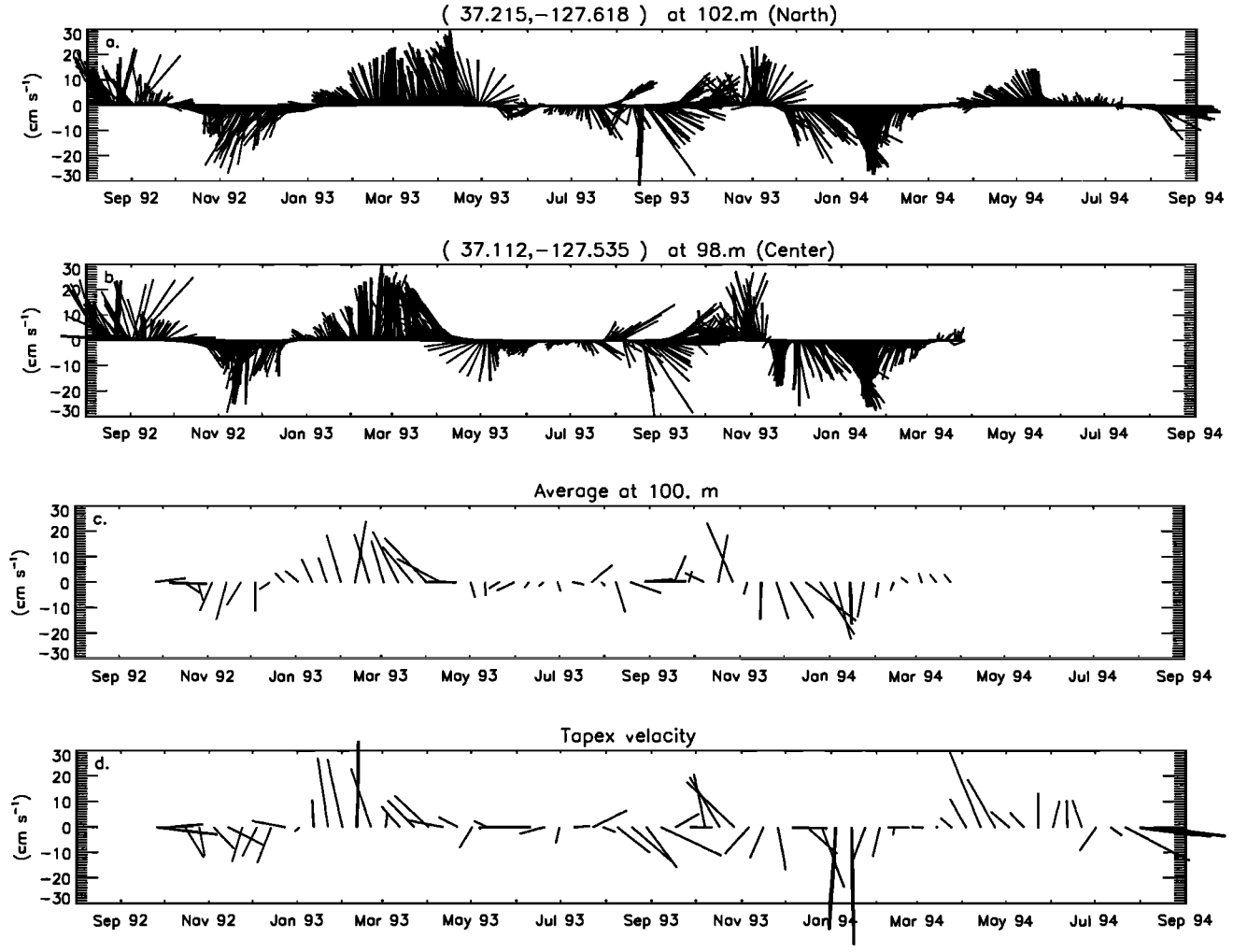

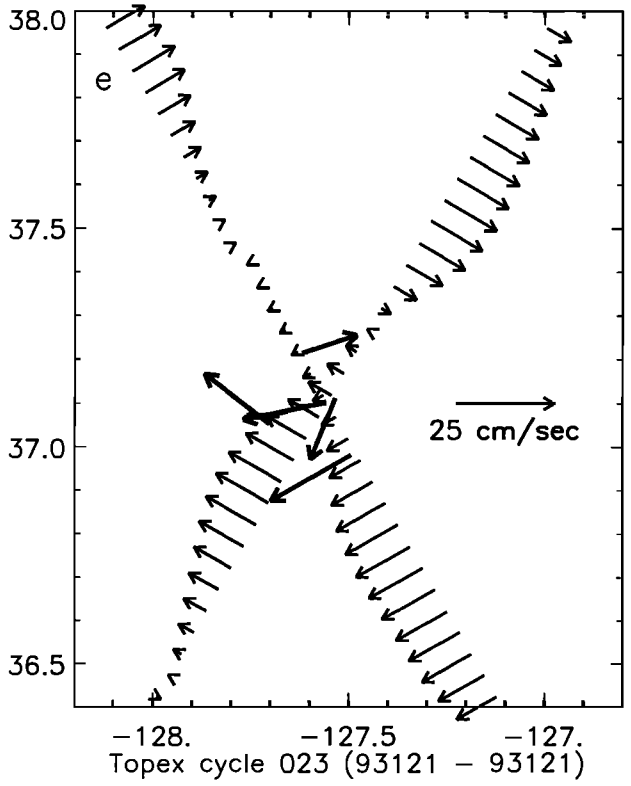

Figure 4. Comparison of velocities from 100-m deep current meters from moorings surrounding the crossover point, August 1992–September 1994. Mean velocities have been removed from the records for the display periods. (a) Daily low-pass filtered velocities from 15 km north of the crossover. (b) Daily low-pass filtered velocities from 2 km northeast of the crossover (central mooring). (c) Ten-day velocities from the average of the four moorings (the central mooring and moorings located 15 km to the north, west, and south of the crossover), subsampled at the altimeter times. (d) Ten-day velocities from the altimeter. (e) TOPEX cross-track velocities and 100-m ADCP (center) and VACM velocities for May 1, 1993. This shows the position of the current meter moorings relative to the altimeter tracks and demonstrates the degree of small-scale variability that can be caused by eddies in the region.

Table 2a. Statistics From Nearby Moorings: Filtered and Subsampled 10-Day Current Meter Data

	σ_u^2, cm^2 s^{-2}	σ_v^2, cm^2 s^{-2}	$\overline{u'v'}$, cm^2 s^{-2}	EKE, cm^2 s^{-2}	Major Axis σ_{11}, cm^2 s^{-2}	Minor Axis σ_{22}, cm^2 s^{-2}	θ, deg
North	81	146	-14	113	148	78	-12
West	77	136	-72	107	184	29	-34
South	92	128	-17	110	134	85	-21
Center	73	144	-19	108	149	68	-14
VACM average	55	125	-34	90	139	41	-22
100-m ADCP	78	110	-17	94	117	71	-24
48-m ADCP	101	149	-6	125	150	100	-7

As in Table 1a.

2-km. To be conservative, we use values of 3–5 cm s^{-1} for the altimeter velocity uncertainty.

Although the TOPEX geostrophic velocities appear accurate, the 10-day sampling creates a Nyquist period of 20 days. The ability of the TOPEX data at crossovers to correctly represent frequency spectra of velocities is thus subject to aliasing of energy with frequencies higher than 0.05 cycle d^{-1}. The data from the current meters provide estimates of the complete spectra of currents (over 1–2 years). Subsampling of the current meters at the 10-day TOPEX sampling times indicates that aliasing is indeed a problem, although not as severe for the spatially averaged currents.

Figures 5a and 5b present the spectra (in energy-preserving form) for the cross-track components of velocity anomalies from the 100-m VACM on the northern mooring (15 km to the north of the crossover point), which has the longest record (2 years), and from the spatial average of all four 100-m VACMs over their common 18-month period. The velocities used are the components in the cross-track direction for the two tracks at the TOPEX crossover. The individual spectra from the two tracks are averaged in each case. The hourly current meter data (after applying the 40-hour half power filter) are used to calculate the full spectra, which are presented in the first three panels for the northern mooring (solid lines) and the spatial average (dotted lines).

Table 2b. Statistics From Nearby Moorings: 10-day rms Difference from TOPEX

	V_{ca}, cm s^{-1}	V_{cd}, cm s^{-1}	u, cm s^{-1}	v, cm s^{-1}
North	8	10	9	8
West	8	9	9	9
South	8	7	7	10
Center	7	8	7	8
Average	7	7	6	8
100-m ADCP	7	6	7	8
48-m ADCP	7	7	7	8

As in Table 1b.

These hourly time series were decimated to the TOPEX 10-day sampling times to produce subsampled spectra (dashed lines) for the spatially averaged velocities (Figure 5a) and the individual northern mooring (Figure 5b). The dashed line in Figure 5c is the spectrum calculated from TOPEX data from the 2-year period coincident with the northern mooring deployment times. In Figure 5d, spectra are presented from the spatially averaged 100-m mooring data, subsampled to TOPEX 10-day times (solid line), from TOPEX data from the same 18-month period as covered by the spatially averaged mooring data (dashed line) and from the full 3 years of TOPEX data (dotted line).

It can be seen that subsampled mooring data produce spectra with artificially enhanced energy at low frequencies, especially for the individual northern mooring (Figure 5b). The same is true of the shorter ADCP record (not pictured). When the hourly current meter data are first filtered with a half power of 20 days, the subsampled data do not produce the higher low-frequency spectra, indicating that the problem is aliased energy with periods shorter than 20 days. It appears to be less severe of a problem for the spatially averaged currents (Figure 5a), for which the spectral slopes at low frequency are approximately correct. This is consistent with the fact that there is less energy at frequencies greater than 0.05 cycle d^{-1} in the full spectrum of the spatially averaged data (Figure 5a) than in the individual mooring (less high-frequency energy to be aliased).

Therefore it seems likely that the TOPEX spectra in Figures 5c and 5d contain aliased high-frequency energy, which

Table 2c. Statistics From Nearby Moorings: 10-day rms Difference Between the Central and Surrounding Moorings

	u, cm s^{-1}	v, cm s^{-1}
North	7	5
West	7	6
South	7	5
100-m ADCP	4	3

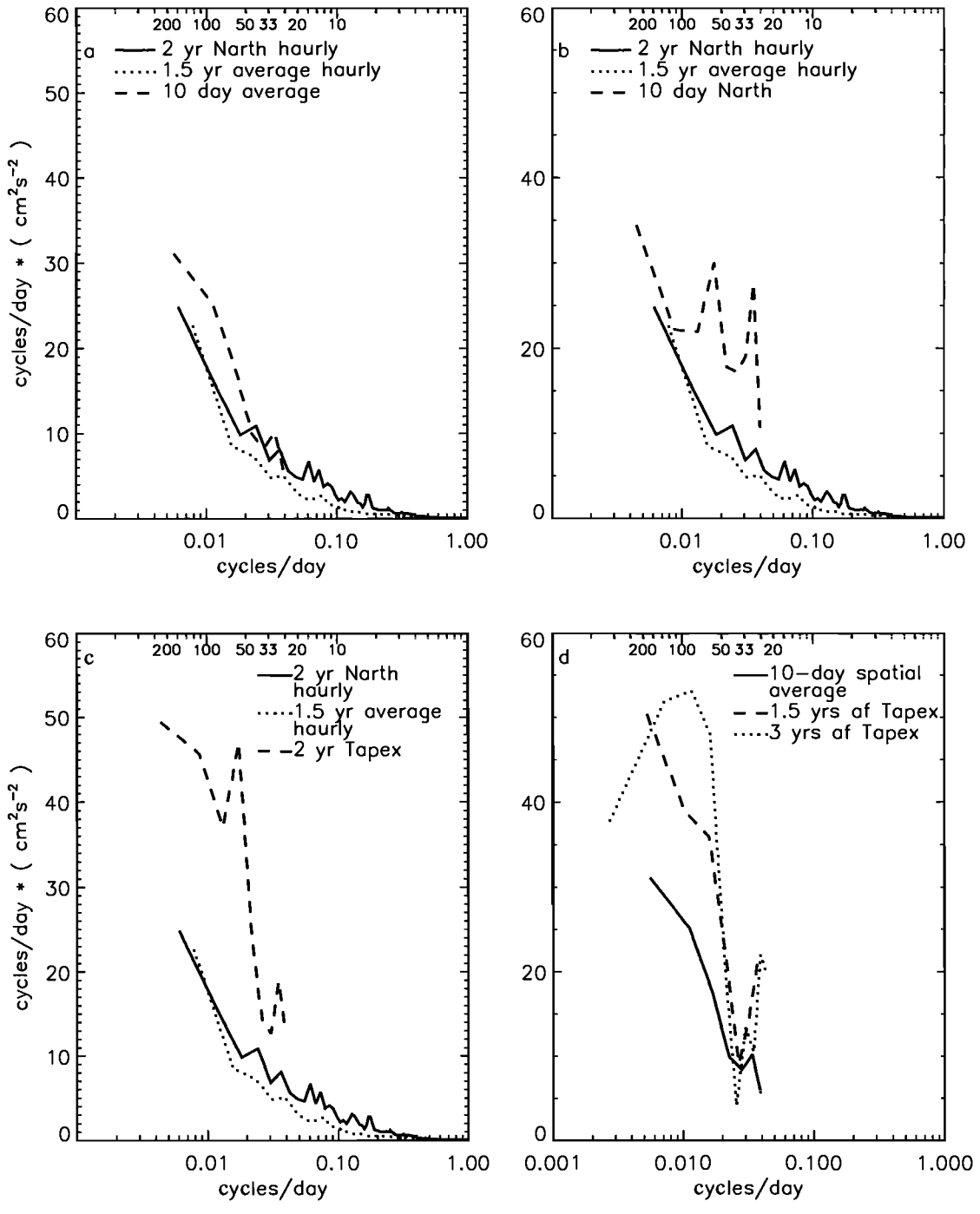

Figure 5. Frequency autospectra for variances of cross-track velocities. Low-pass (40-hour half power) filtered measured currents from 100 m, measured currents subsampled at the 10-day TOPEX crossover times, and TOPEX current estimates. All spectra are averages of the two individual spectra from the ascending and descending cross-track components. Spectra are presented in energy-preserving form. (a) Spectra from 24 months of hourly measured currents from the mooring 15 km north of the crossover (solid line) and from 18 months of spatially averaged hourly measured currents from the four moorings (dotted line), and the same spatially averaged currents subsampled at the 10-day TOPEX crossover times (dashed line). (b) As in Figure 5a, except for the dashed line, which is now the 10-day subsampled data from the northern mooring. (c) As in Figure 5a, except for the dashed line, which is now the 10-day TOPEX velocities, over the same 24 months used for the northern mooring. (d) Spectra for the subsampled, spatially averaged measured currents (solid line), from TOPEX using the same 18 months as for the spatially averaged measured currents (dashed line), and from the full 3-year TOPEX record (dotted line).

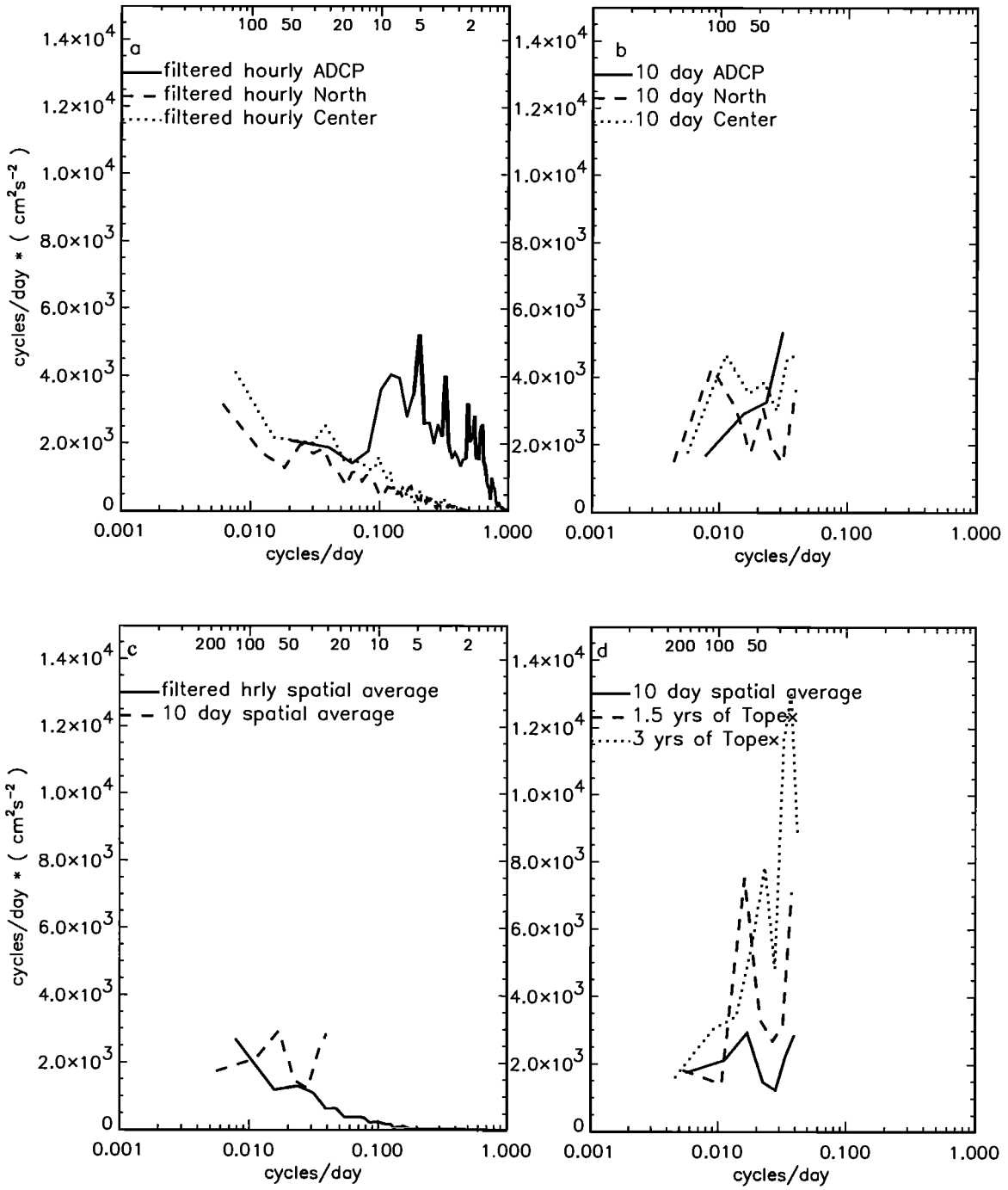

Figure 6. Frequency spectra for covariances, presented in energy-preserving form. (a) Low-pass filtered hourly measured currents from the ADCP velocity at 48-m depth (solid line), from the northern mooring at 100 m (dashed line), and from the central mooring at 100 m (dotted line). (b) Low-pass filtered measured currents subsampled at the 10-day TOPEX crossover times for the ADCP velocity at 48-m depth (solid line), from the northern mooring at 100 m (dashed line), and from the central mooring at 100 m (dotted line). (c) Low-pass filtered, hourly, spatially averaged measured currents at 100 m (solid line) and the same data, subsampled at the 10-day TOPEX crossover times (dashed line). (d) Covariance spectra from the 18 months of spatially averaged measured currents, subsampled at the 10-day TOPEX crossover times (solid line), from TOPEX data over the same 18-month period (dashed line), and from TOPEX data over the full 3-year period (dotted line).

cannot be removed. What aspects of the TOPEX spectra in Figure 5d are realistic? The 18-month TOPEX data produce a spectrum with similar shape around periods of 100 days to the spatially averaged 100-m current meter record, although with higher energy. The higher TOPEX energy is consistent with the fact that it represents surface currents, given the decrease in energy between the 48 and 100-m ADCP currents. When the full 3 years of TOPEX data are

used, a peak is observed with periods around 100–150 days. This peak is consistent with previous measurements in the same region [*Stabeno and Smith,* 1987] and with the visual interpretation of dominant time scales in Figures 2 and 4. Thus although aliased, the three-year TOPEX time series appears to resolve the 100–150 day periodicity evident in Figures 2 and 4. TOPEX and current meter records show that 2 years of data are not long enough to resolve this peak.

The spectra calculated from the covariances ($\overline{u'v'}$, Figure 6a) are even more difficult to interpret. The ADCP currents from 48-m depth produce a broad peak of energy with periods between 2 and 10 days. ADCP currents from 100-m depth produce a less energetic peak at the same periods (not shown). The individual VACM data (Figure 6a) and their spatial average (Figure 6c) do not produce this peak. As noted above, the burst sampling of the ADCP data (5 min of 1 Hz data every 20 min) was designed to reduce the influence of surface waves (and conserve battery power) but allows aliasing of internal waves with periods of 5–40 min. These waves would not be aliased by the VACM 30-min vector averages.

Using only the VACM data, subsampling the individual 100-m current meter data at the TOPEX 10-day sampling rate produces covariance spectra that do not capture the mildly red nature of the hourly covariance spectra (Figure 6b). Subsampling the spatial average of the current meter data also fails to capture the shape of the covariance spectrum (Figure 6c), although the area under the curve is not greatly in error. Covariance spectra from 18 months of TOPEX data are more energetic than the covariance spectrum from the subsampled spatially averaged 100-m data, with peaks and troughs similar to the subsampled current meter data (Figure 6d) but different from the covariance spectrum from the full record of filtered hourly data (Figure 6c). The full 3 years of TOPEX data produce a covariance spectrum that is even higher in energy and blue. Given the uncertainty caused by the aliasing of the measured currents, we place no confidence in the shape of TOPEX covariance spectra. This aliasing of the covariance spectra may explain why the momentum flux statistics are the most variable when the record length and subsampling characteristics are changed.

3.3. Horizontal Resolution

Tracks 130 and 69 (Figure 1) are used to compare the spatial structure of the cross-track velocities to the spatial structure in the SST fields. We have already noted the general sense in which the cross-track velocities and SST patterns in Figure 1 are consistent with the thermal wind relation. In Figure 7 we show linear regressions of V_c against $-\Delta T$ during cycle 2 for these two tracks, i.e., $V_c = A_0 - A_1 \Delta T$. We define V_c to be positive if it is directed toward the east and ΔT to be positive if temperature increases toward the north. Thus positive velocities correspond to temperatures and surface heights decreasing toward the north, if the thermal wind relation holds. The regressions quantify the agreement between the two sides of (4), keeping Z_r constant within each track but allowing it to vary between tracks. The temporal separations between altimeter and AVHRR data are 2 and 4 days for tracks 130 and 69 during cycle 2, respectively. Considering all of the data examined, we find no relation between temporal separations of up to 5 days and the agreement between altimeter and AVHRR data (other factors are more important than the offset in time).

In Figure 8 we show along-track plots of V_c for the same tracks during cycles 1 and 2 (late September and October), compared to $-A_1 \Delta T$ in regions where the AVHRR image

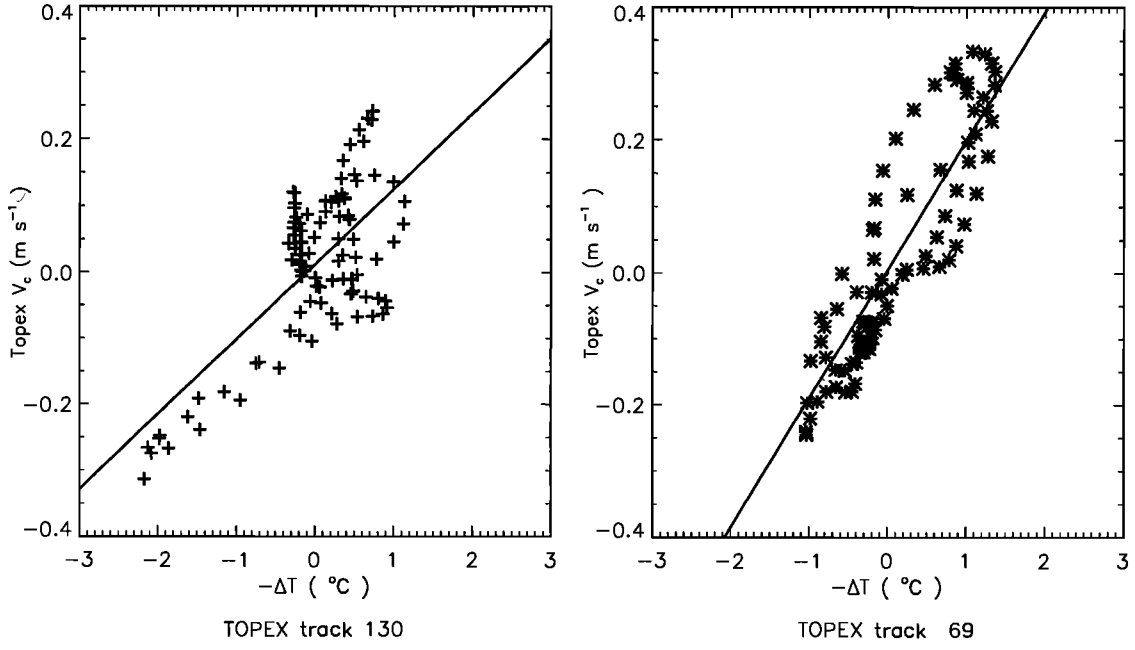

Figure 7. Linear regression scatterplot, cycle 2, tracks 130 and 69: TOPEX V_c versus $-\Delta T$. The AVHRR image is from October 9, 1992. The TOPEX tracks are from October 8 (track 130) and October 5, 1992 (track 69).

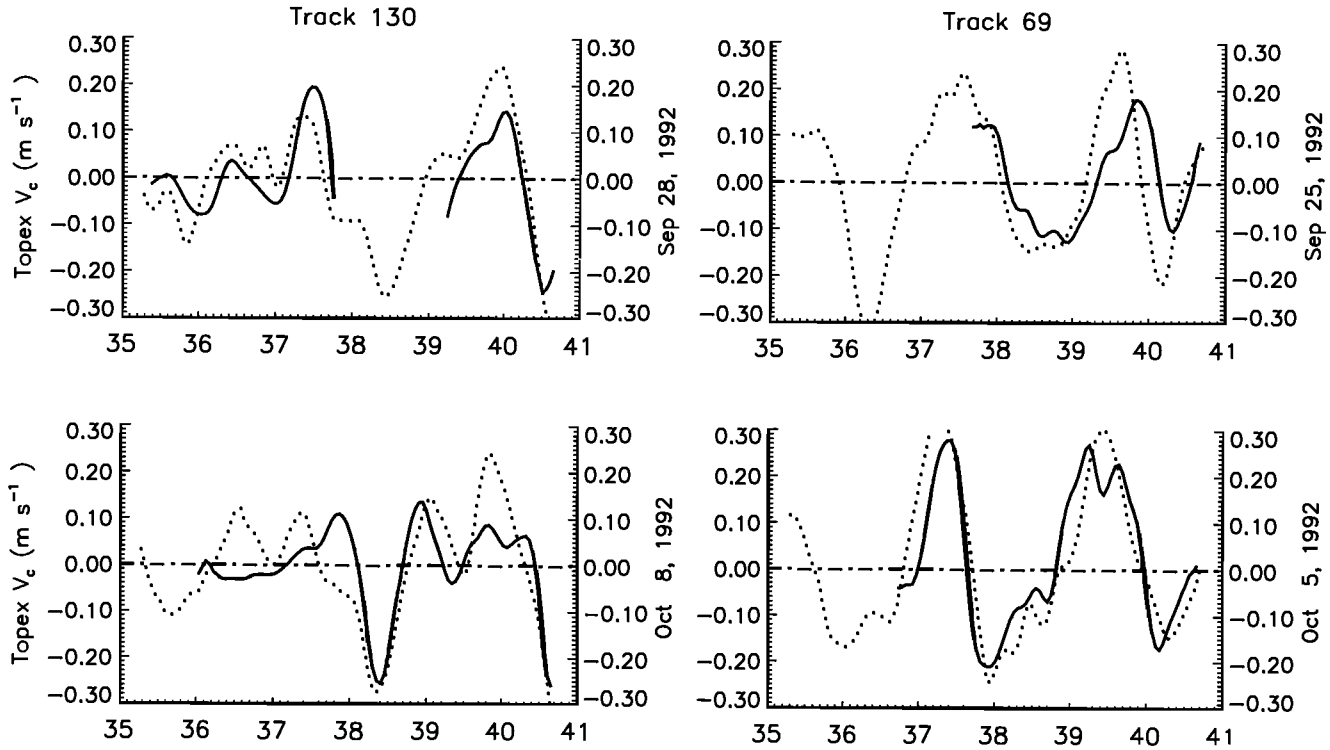

Figure 8. Along-track plots of TOPEX V_c (dotted line) and $-A_1\Delta T$ (solid line) for cycles (top) 1 and (bottom) 2 for tracks 130 and 69 (dates of tracks to the right of each panel). The SST gradients come from AVHRR images on September 24, 1992 (cycle 1), and October 9, 1992 (cycle 2).

was judged to be clear. These are the data used in the Figure 7 regressions. Figures 1, 7, and 8 allow several kinds of qualitative, visual determinations of the horizontal scales resolved by the altimeter: by comparison of V_c to the pattern of SST gradients (Figures 1 and 8) in regions where the thermal wind relation appears valid, as judged by the regressions in Figure 7; and by the scales of the features in altimeter velocities that were temporally persistent from cycle to cycle.

Table 3 presents the values of the regression coefficient, A_1, the correlation coefficient, r, r^2 (as the percent of variance explained), and the temporal separation between al-

Table 3. Regressions of Cross-Track Velocity and Along-Track SST Gradient

TOPEX Cycle	AVHRR Date	A^1	r	$r^2 \times 100$	Temporal Separation
		TOPEX Track 130			
1	9-24-92	0.158	0.811	65.7%	3 days, 6 hours
2	10-9-92	0.114	0.711	50.5%	-1 days, 21 hours
8	12-4-92	0.098	0.610	37.3%	2 days, 3 hours
9	12-13-92	0.117	0.498	24.8%	3 days, 13 hours
10	12-23-92	0.145	0.628	39.5%	2 days, 11 hours
15	2-13-93	0.191	0.635	40.4%	2 hours
17	3-3-93	0.160	0.579	33.5%	2 days, 5 hours
23	4-29-93	0.125	0.560	31.3%	5 days, 5 hours
29	6-29-93	0.161	0.878	77.0%	2 days, 21 hours
		TOPEX Track 69			
1	9-24-92	0.162	0.756	57.2%	18 hours
2	10-9-92	0.195	0.875	76.6%	-4 days, 5 hours
8	12-4-92	0.115	0.837	70.1%	-7 hours
9	12-13-92	0.134	0.615	37.8%	3 hours
10	12-23-92	0.073	0.479	22.9%	2 hours

timeter tracks and the SST image. These statistics are presented only for the regressions along the two longer tracks of interest during cycles where the record of ΔT was judged to be cloud-free along a path of approximately 300 km or more. Spatial decorrelation scales are 50-80 km and result in approximately 4-10 degrees of freedom for records of 300-500 km in length, with corresponding 95% significance levels of 0.75 to 0.58. We use these statistics primarily to indicate where the temperature gradient patterns may be better or worse indicators of the velocity patterns.

During cycles 1 and 2, for example, the temperature gradients appear to give a relatively good picture of the velocity structure along tracks 130 and 69 (explaining 51 to 77% of the variance), with correlations that are significant. Altimeter velocities in Figures 1 and 8 depict a consistent picture of offshore (negative) flow north of 40.0°–40.5°N, onshore flow between 39°and 40°N, offshore flow between 38°and 39°N, and onshore flow between 36.5°and 37.5°N, which is also indicated along tracks 145 and 54 in Figure 1. The poorest agreement between SST gradients and TOPEX velocities occurs in the SE part of the region during cycle 2, where the southern part of track 130 lies in a region of low-temperature gradients (as indicated by Figure 1). In Figure 7, these regions contribute to the large number of points with $\Delta T \approx 0$ which lie off the regression lines for track 130. Undetected clouds and mist may contribute to the lack of SST features, as may subduction of the colder jet water in this region [*Brink and Cowles,* 1991]. The persistence of the altimeter cross-track velocity features during sequential cycles 1–2 (with some strengthening, weakening, and shift in position) argues for the validity of those features. In the top left panel of Figure 8, oscillations in velocity with wavelengths of approximately 30 km are seen along track 130 in cycle 1 between 36°and 37°N, which cannot be distinguished from noise due to their lack of persistence and correspondence to the SST gradients. In contrast, the oscillations with scales of 50–80 km are persistent over pairs of cycles and assumed valid. Overall, the figures suggest that velocity structures with scales of 50–80 km and larger are resolved by the altimeter.

Values of A_1 in Table 3 are most often between 0.1 and 0.2. Using (4) and typical values for g, f, and β (assuming no influence of salt on density), the value of Z_T implied by these values of A_1 is approximately 300–600 m. These values are of the same order of magnitude as the 600-m depth of the "level of no motion" which *Walstad et al.* [1991] found to give the best agreement between geostrophic calculations and ADCP fields in this region, although *Walstad et al.* make the point that no single "level of no motion" is optimum for a regional velocity field.

During winter, the circulation in this region consists of a poleward Davidson Current next to the coast, carrying warmer water to the north. In the offshore region, the field of eddies from summer and fall continues to evolve and dissipate. The late January picture of SST and cycle 14 altimeter velocities shown in Figure 9 depicts the warmer band of poleward flow next to the coast. SST gradients are weaker, with a somewhat more confused pattern of offshore SST patterns and cross-track velocities than found in late summer and fall. Close inspection, however, reveals a continued correspondence of SST and velocity features. A warm anticyclonic feature is centered around 40°N, 126.2°W. The colder water farther offshore of this feature may be a remnant of the cyclonic meander found in Figure 1 around 40.2°N, 127°–128°W. Likewise, the cold cyclonic meander between 37°and 39°N, 126°and 127°W in Figure 1 may have evolved into the cool feature with cyclonic flow found between 36°and 38°N, 127°and 129°W in Figure 9, with a separate cool feature found inshore of this between 36°and 38°N, 124.5°and 126.5°W. The linear regressions for cycles 13 or 14, plotted in Figure 10, show the generally smaller range of ΔT values that exist in winter. The regressions explain less of the variance (27%–46%) than those from early fall. As in Figure 7, many of the points which do not fit the regressions of Figure 10 are for values of $|\Delta T| \leq$ (0.5° to 1.0°C). Plots of V_c and $-A_1 \Delta T$ for cycles 14 and 15 are shown in Figure 11. The anticyclonic feature between 39°and 41°N, 126°and 127°W, and the cyclonic feature between 36°and 38°, 127°and 129°W N can be seen in the altimeter signals and in some of the SST gradients. The persistence of the larger signals in the altimeter velocities gives the overall impression that although the structure seems less organized in Figure 9, there is still agreement between the strongest features in the SST patterns and the altimeter velocities, which still resolve features with scales of 80 km and greater in winter.

One problem with the comparison between the cross-track velocity and along-track temperature gradient is the fact that the "long-term" mean temperature that is removed at each point may have a different number of realizations at different spatial points along the track, which can create unrealistic features in the gradients. Similar problems occur in the TOPEX data but are far fewer due to the smaller number of missing data. We can avoid this by forming the difference between two individual cycles (along a given track), without taking out a long-term mean. This difference represents the change in cross-track velocity at each point. This removes the artificial velocities caused by the geoid (which should be the same for the two altimeter records), uses data only where there are good data during both cycles, and creates no artificial signals. Comparison of differences between 11 pairs of cycles along track 130 and four pairs along track 69, with no long-term mean removed, results in similar or better agreement between $\Delta(V_c)$ and $\Delta(-A_1 \Delta T))$ as the comparisons between V_c and ΔT during individual cycles (with the long-term mean extracted). Plots of $\Delta(V_c)$ and $\Delta(-A_1 \Delta T))$ for four of the cycle pairs are presented in Figure 12. These generally show good agreement, resolving the features with scales of 50–80 km.

4. Discussion and Conclusions

Below we give the major methodological and oceanographic conclusions, along with a discussion of points which need elaboration or clarification. The Appendix includes a discussion of how details of the geostrophic calculation influence the scales of circulation features that are resolved.

4.1. Methodological Conclusions

1. Considering accuracy, the level of noise in the altimeter velocities is 3–5 cm s^{-1} or less, corresponding to noise in the altimeter heights of approximately 2 cm. Results of

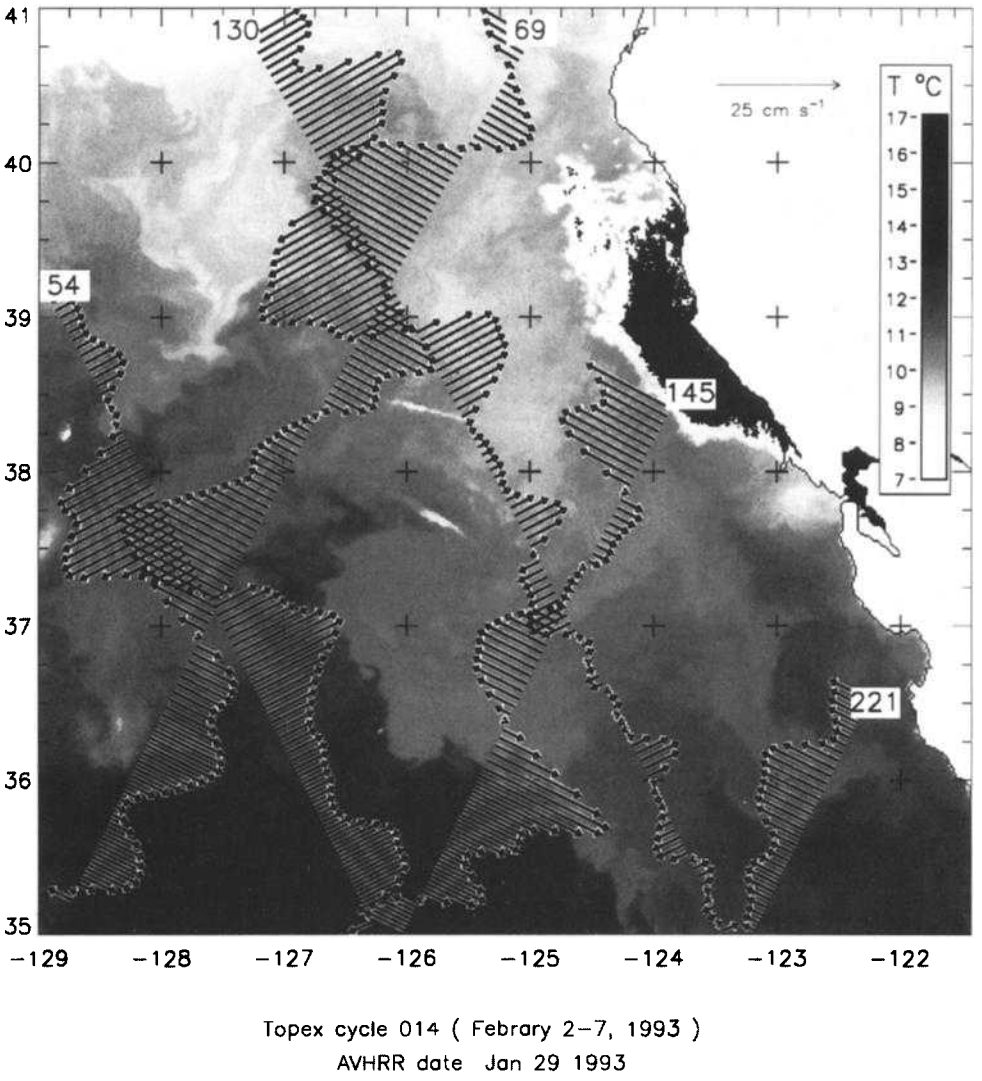

Figure 9. A characteristic winter field of TOPEX cross-track velocities (cycle 14) overlain on an SST image (January 29, 1993). As in Figure 1.

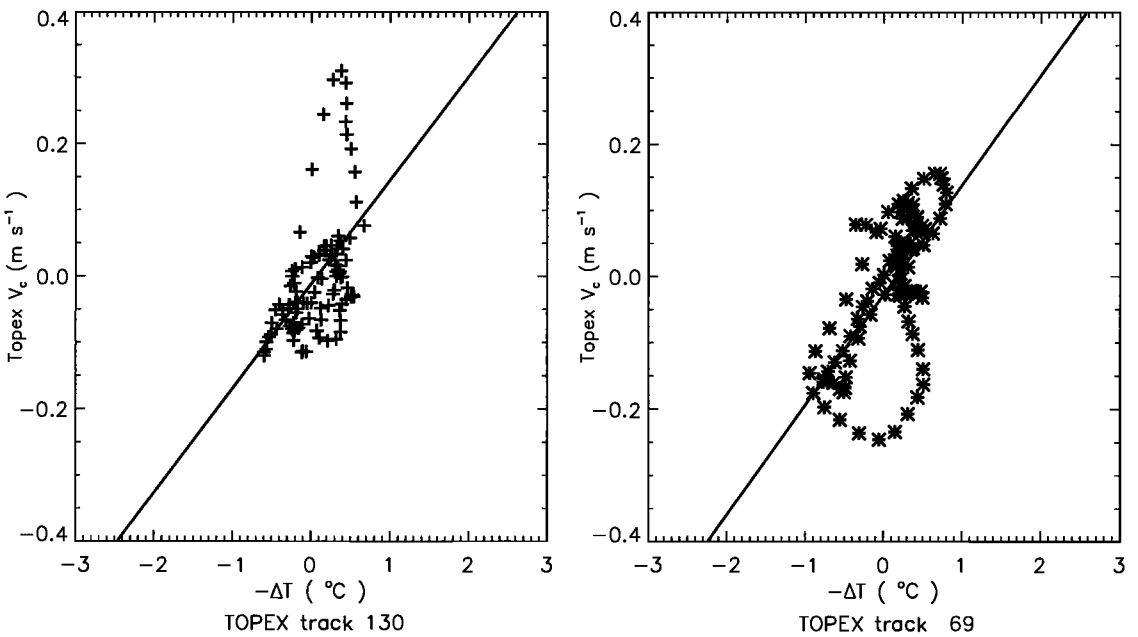

Figure 10. Linear regressions as in Figure 7, for cycles (left) 13 and (right) 14. The AVHRR image is from January 29, 1993. The TOPEX tracks are from January 25, 1993 (track 130), and February 1, 1993 (track 69).

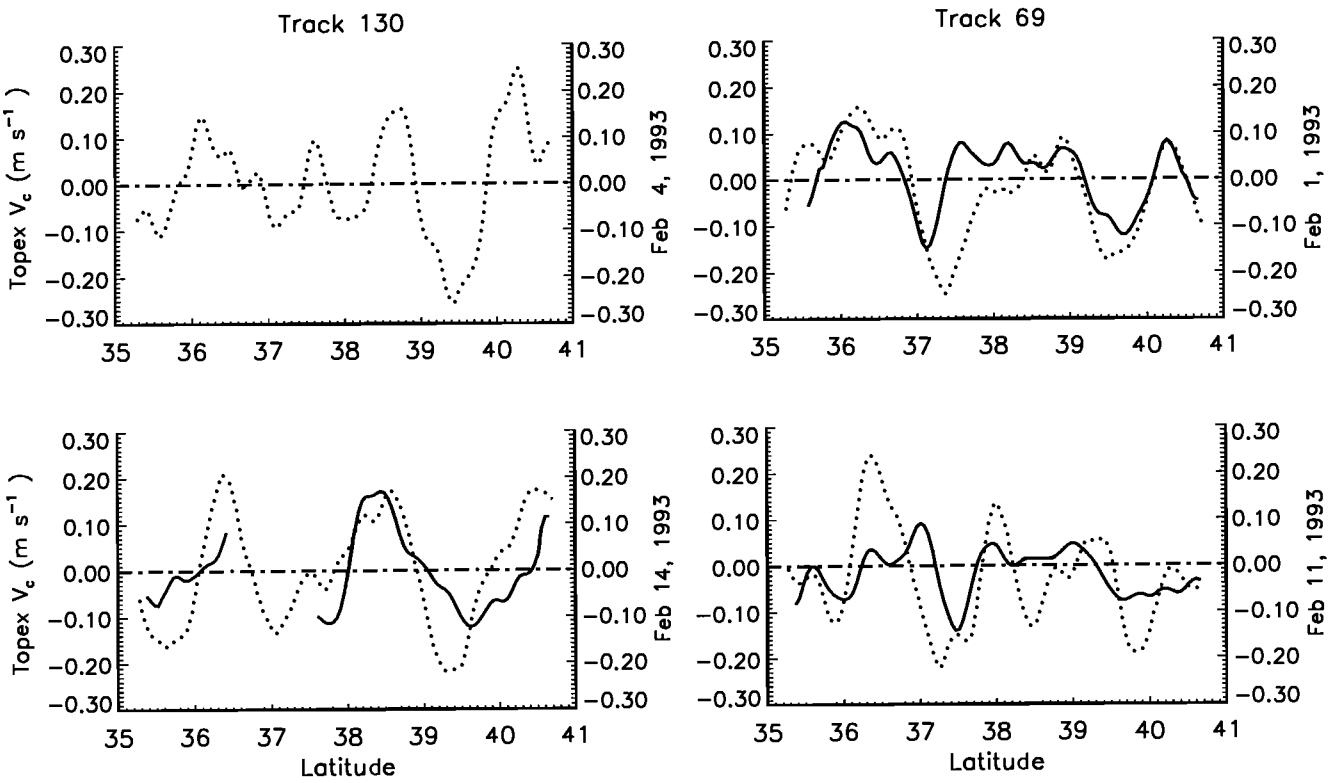

Figure 11. Along-track plots of TOPEX V_c (dotted line) and $-A_1\Delta T$ (solid line) for cycles (top) 14 and (bottom) 15 for tracks 130 and 69 (dates of tracks to the right of each panel). The SST gradients come from AVHRR images on January 29, 1993 (cycle 14), and February 13, 1993 (cycle 15).

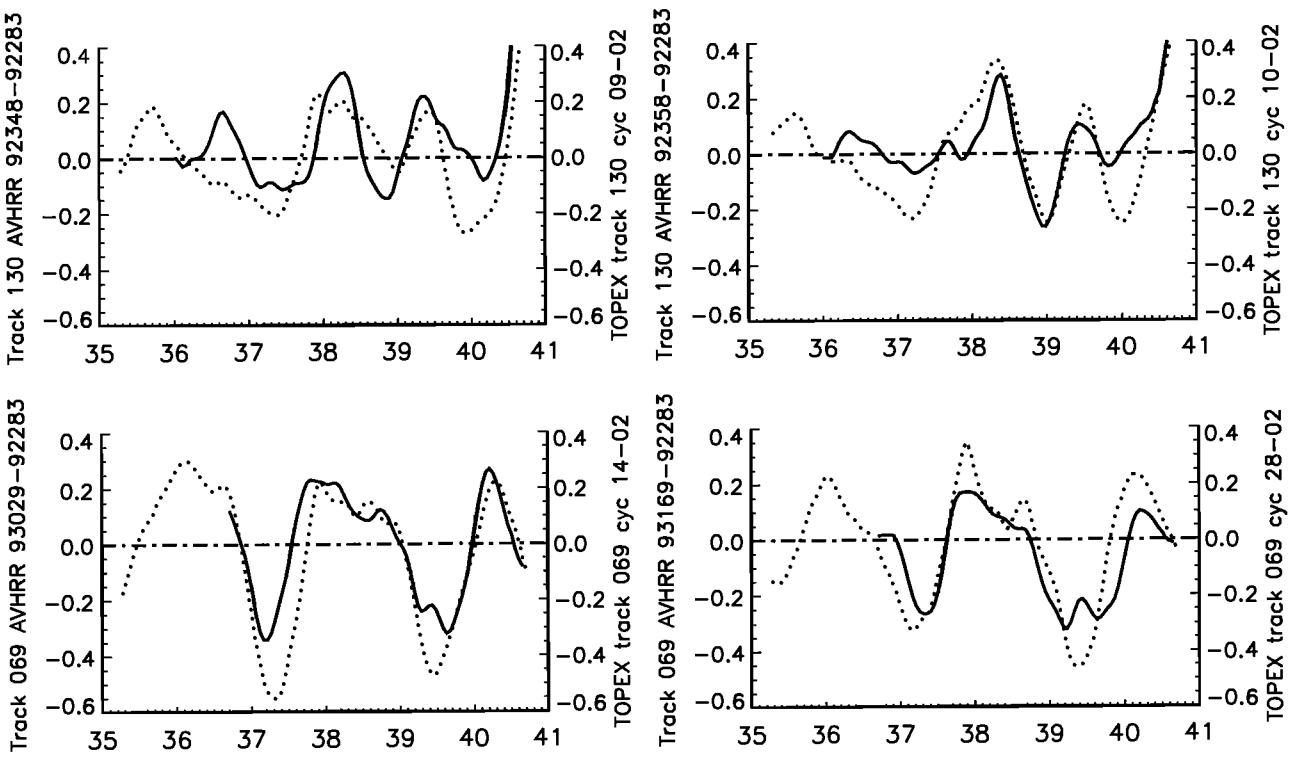

Figure 12. Differences between V_c for pairs of cycles and differences between $-A_1\Delta T$ for the same pairs of cycles. AVHRR dates are to the left of each panel and cycle numbers are to the right.

comparisons between altimeter geostrophic velocities and velocities measured beneath the Ekman layer depend on details of the geostrophic calculation, as described in the Appendix. For a 62-km finite difference, followed by a 50-km spatial filter, the total rms difference is 7–8 cm s^{-1}. This improves slightly when the measured velocities are spatially averaged over a 30-km region, showing that the altimeter measurement is representative of spatially averaged velocities rather than point measurements. Of this rms difference, small-scale horizontal circulation features in the ocean cause 5–7 cm s^{-1} rms differences between current meters separated by 15–30 km. Another 5 cm s^{-1} rms difference exists between current meters at 48 and 100-m depth, showing the effects of vertical spatial variability (shear). Thus of the total rms difference, less than 3–5 cm s^{-1} can be attributed to noise in the altimeter calculation, similar to the difference between the 100-m currents measured by the ADCP and VACM when separated by 2 km. This shows a greater accuracy than previous estimates of 10–17 cm s^{-1} by *Menkes et al.* [1995], using current meters at the equator. In the Appendix it is shown that the full rms difference of 7.6 cm s^{-1} corresponds to height errors of 3.3 cm rms, while a 3–5 cm s^{-1} difference corresponds to height errors of approximately 2 cm and less. These values are similar to the rms height errors found by *Katz et al.* [1995] and *Picaut et al.* [1995], based on temperature and conductivity moorings in the equatorial Pacific.

2. With respect to temporal resolution, the altimeter 10-day sampling appears capable of resolving the dominant 100–150 day periods of variability in the offshore region of the California Current, as seen by visual comparisons of altimeter and current meter data (Figures 2 and 4) and by spectral analysis of the 3-year TOPEX record (Figure 5d), although aliasing of higher-frequency energy does affect spectral calculations of the TOPEX data. The measured velocities are used to calculate full autospectra (after the 40-hour filter) and autospectra after subsampling the same data at the TOPEX 10-day period. Energy at frequencies below the Nyquist frequency (0.05 cycles d^{-1}) increases for the subsampled spectra, although less so when the spatial average (over a 30-km region) of the measured velocities is used. TOPEX data represent averages over longer spatial scales and their autospectra appear similar in slope to the full spectra from the spatially averaged measured velocities over an 18-month common period, giving some confidence in the spectral characteristics calculated from TOPEX data. Over a 3-year period, the TOPEX autospectra resolve a peak with a 100–150 day period, similar to the visual interpretation of timescales in all of the velocity data. A spectral peak at 70–100 days has been found in deeper (1250 m) measured velocities at a nearby deep ocean location by *Stabeno and Smith* [1987], giving further confidence in the peak resolved by the longer record. The 2-year records of measured and TOPEX velocities are not long enough to resolve this peak. The fact that the spatially averaged measured velocities exhibited less severe aliasing argues for the use of larger spatial filtering (approximately 100 km) in making the geostrophic velocity calculation from TOPEX heights, prior to spectral analysis. Similarly, spatial averaging of altimeter heights, such as the 2° averages used by *Wunsch and Stammer* [1995], seems likely to reduce effects of aliasing in their frequency spectra of height variance.

3. Regarding spatial resolution, the TOPEX cross-track velocities can repeatedly resolve features with horizontal scales of 50–80 km, as demonstrated by comparisons between the along-track gradients of SST and the cross-track geostrophic velocity from the altimeter. Given the 62-km horizontal spacing of the finite difference in heights and the 50-km spatial filter used to calculate the geostrophic velocities, this agreement is as good as can be expected. This raises the question of whether shorter finite differences and spatial filters could be used to improve the resolution. In the Appendix we show that shorter finite differences, followed by the 50-km loess filter, increase the rms differences between measured velocities and TOPEX from 8–9 cm s^{-1} (span of 50 km) to 14–17 cm s^{-1} (span of 12.4 km). Use of shorter spans with no filter increases the rms differences from 8 cm s^{-1} (span of 62 km) to 20–30 cm s^{-1} (span of 12.4 km). The 50-km filter is less important for the longer spans, but it appears that gradient operators with spans of 50–60 km are necessary to achieve the lower rms differences of 7–8 cm s^{-1} between altimeter and measured currents. Error levels associated with other gradient operators are discussed further in the Appendix.

4. Eddy statistics are more problematic. The most robust eddy statistics are the values of EKE, the velocity variances, and the lengths of the major axes of the principal axis ellipses. The magnitude of the momentum fluxes and the orientation of the principal axis of the TOPEX data show greater disagreement with those of the in situ current measurements, but the agreement is much greater with the spatial average of the in situ measurements. Thus, a good part of the differences is due to real variability between surface and deeper features and real, small-scale horizontal variability in the measured currents. We feel that analyses of the spatial and temporal fields of EKE and velocity variance will produce results similar to that which would have been obtained by an array of current meters.

Principal axis ellipses are more complex than the scalar values of EKE and velocity variance. *Morrow et al.* [1994] use a simple approach to estimate the overall uncertainty in the principal axis ellipses, which rejects ellipses with major axes of less magnitude than the largest error variance expected at that latitude. We use this method with our estimates of the rms cross-track velocity errors, as calculated from (2a) and (2b). In Figure 13, principal axes ellipses are shown as calculated from the 3 years of TOPEX data over the large-scale California Current regime. The error variances calculated from (2a) and (2b), using $\sigma_{vc} = 50$ cm^2 s^{-2}, are shown on the right axis for reference, adopting a conservative estimate of altimeter noise as 7 cm s^{-1}. Using 5 cm s^{-1} would result in error ellipses half as large. All "significant" principal axis ellipses (with major axis greater than the larger error variance) are indicated by dark shading.

Figure 13 demonstrates a number of aspects of the velocity statistics in this region. The largest ellipses are found at the one or two crossovers closest to the coast (within approximately 500 km of the coast), i.e., the region of the energetic seasonal jet found in numerous surveys and in drifter tracks [*Brink and Cowles,* 1991; *Brink et al.,* 1991]. Offshore of

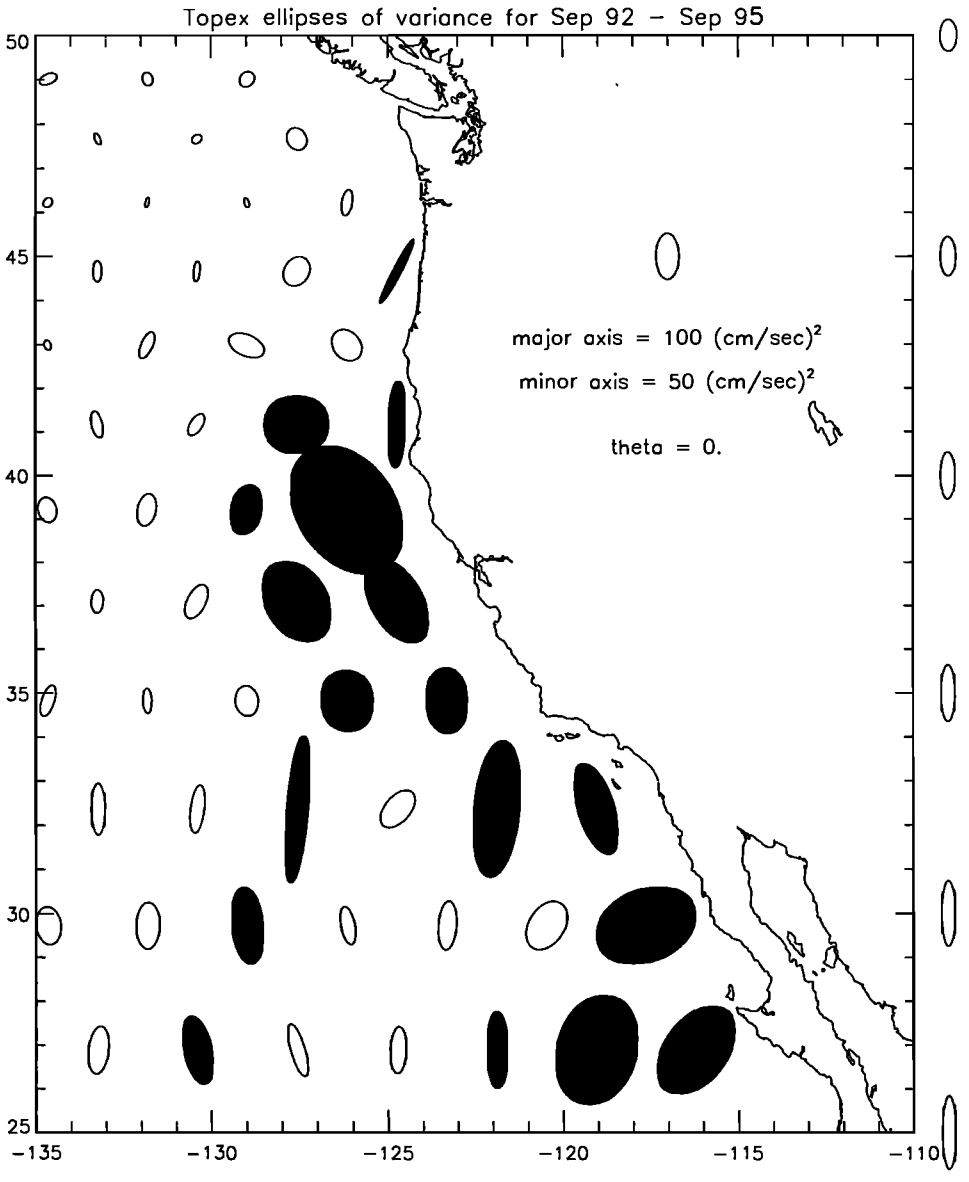

Figure 13. Principal axis ellipses for all TOPEX crossover points in the region of interest, using all 3 years of TOPEX data. Uncertainty variance ellipses are drawn along the right axis, showing the uncertainty in u (horizontal axis) and v (vertical axis), as calculated from (2a) and (2b), using σ_{vc}^2= 50.0 cm^2 s^{-2}, corresponding to an rms uncertainty of 7 cm s^{-1}. Ellipses with major axes greater than the uncertainty are shown darkened.

this region, the variances are low. This is the "eddy desert" pointed out by numerous analyses of altimeter and other data as typical of eastern boundary currents. Considering the smaller ellipses, south of 35°–45°N the north-south polarization becomes more pronounced, similar to the error variance ellipses. These low-energy ellipses in the offshore region provide, in effect, an empirical estimate of principal axis ellipses due to altimeter noise, supporting values less than 7 cm s^{-1}. The lower values offshore also highlight the more energetic region of the California Current. Thus the evaluation of altimeter velocity error is helpful in defining the signal of interest in the region, which is the subject of subsequent papers.

Turning to the more problematic eddy statistics, the values of eddy momentum flux ($\overline{u'v'}$) vary between TOPEX and ADCP velocities by a factor of 6 and vary between 100-m-deep VACMs separated by 15–30 km by a factor of 5. Spectra of ($\overline{u'v'}$) indicate that one problem is aliasing of higher-frequency variability, and at present we have no confidence in these covariance spectra. The agreement between values of TOPEX $\overline{u'v'}$ (-40 to -24 cm^2 s^{-2} for 1- and 3-year records) and the 100-m VACMs is improved by using spatially averaged VACM velocities (-34 cm^2 s^{-2}). These numbers suggest an estimate of -30 ± 10 cm^2 s^{-2} at this location as a representative estimate of the mean eddy momentum flux. The analysis also indicates that the geostrophic velocity calculations should use gradient operators with larger spatial differences and cover the longest period available to try to stabilize the statistics. The orientation of the principal axis for the spatially averaged measured

currents (-22°) is also more like the TOPEX estimate (-30°). We thus end with greater confidence in the TOPEX eddy statistics (other than the covariance spectra) as representative of oceanic currents when averaged over spatial scales of approximately 50–100 km.

4.2. Oceanographic Conclusions

1. The velocity components in the California Current are anisotropic and may be strongly polarized, even at locations 400 km from the shelf break over the deep ocean. The statistics in Tables 1a and 2a indicate that the minor axes of the principal axis ellipses are smaller in magnitude than the major axes by factors of 1.5 (hourly filtered ADCP) to 4 (spatial average of 100-m VACMs). TOPEX at the same location shows a factor of 1.25 to 2, depending on the period used. Figure 13 shows a similar level of polarization in the ellipses judged significant. Thus estimates of EKE based on cross-track velocity variances that assume isotropy are in error in some locations.

2. Persistent, small-scale variability occurs in the offshore region of the California Current System, with opposing velocities ($\pm$ 20 cm s^{-1}) found at distances of 15–30 km, lasting several weeks. Figure 4e demonstrates this at the mooring sites from measured currents at 100-m depth. An anticyclonic eddy appears to have drifted over the mooring site, creating these small-scale velocity differences. The choice of numerical operators used in calculating altimeter velocities should take this small-scale variability into account.

3. Small principal axis ellipses indicate low eddy energy levels at crossovers located 700 km and more from the coast, isolating the more energetic region within approximately 500 km of the coast. Surface drifters and field surveys also find energetic eddies and meandering jets within 500 km of the coast. The isolation of this region supports the hypothesis that the observed eddies are derived from the California Current, rather than being deep ocean eddies that move onshore into the California Current System.

Appendix: Geostrophic Calculations

Our calculation of the geostrophic velocity from along-track gradients of altimeter heights begins with a centered, finite difference form of the geostrophic calculation.

$$V_c(j) = -\frac{g}{f}\frac{\partial h}{\partial s} = -\frac{g}{f}\left[\frac{h(j+n) - h(j-n)}{2n\ \Delta s}\right] \quad \text{(A1)}$$

where V_c is the cross-track surface velocity (positive to the right of the track, when looking along the track from south to north), g is the acceleration of gravity, f is the Coriolis parameter, h is the corrected sea surface height, s is the along-track coordinate, j is the index of the along-track grid point, numbered from south-to-north, and n is the half span of the centered difference. The resulting velocities are then smoothed with a spatial filter and the mean velocity from the total period is removed at each grid point to eliminate the influence of the marine geoid.

In the present calculations, we use a span of 10 TOPEX intervals (n=5) to produce a 62-km difference and then filter with a loess filter with a half span of 50 km, as given by *Chelton et al.* [1990]. The 62-km difference is a high-pass filter, reducing the energy by half for scales of motion greater than approximately 250 km. The loess filter eliminates energy by a factor of 2 for scales of motion less than 80 km, eliminating the minor effects of the high-frequency sidelobes of the difference operator. The combination of the two filters reduces the energy of signals by an order of magnitude outside of the range between approximately 60 and 625 km. At the edges of tracks or around missing data points, where the number of points is less than needed for the loess filter, we substitute a simple three-point running mean. This is a low-pass filter with a half power point of approximately 30–40 km. Although the running mean has a less aesthetically pleasing set of high-frequency sidelobes, there is almost no difference between statistics calculated using the running mean everywhere and those calculated using the loess filter. In fact, neither the loess filter nor the three-point running mean change the statistics of the comparison to current meters substantially, although they make the along-track velocity fields look smoother.

The choice of these parameters is based on experience with Geosat data and further tests with TOPEX data. During the Geosat Exact Repeat Mission, hydrographic surveys were conducted off northern California in spring and summer of 1987 and 1988 as part of the Office of Naval Research-sponsored coastal transition zone initiative. Surveys in May–June 1987 were coincident with Geosat data along ascending tracks which ran parallel to the coast approximately 100 and 250 km offshore. Use of these data and coincident AVHRR temperature gradients (tests similar to those reported in section 3) gave an initial indication that the altimeter could resolve mesoscale features of 50–100 km. The hydrographic data allowed more quantitative tests of various methods of calculating the along-track height gradients. These tests resulted in the use of a centered difference with a 63-km span, followed by a three-point running mean. With TOPEX data, 10 grid intervals on the tracks produced by JPL produce a 62-km difference, and we have replaced the running mean with the loess filter except where the number of points is limited.

The effects of varying the finite difference and smoothing operators were further tested during the present study, based on changes in the rms difference between the TOPEX velocities at the crossover and the spatially averaged 18-month record of 100-m current measurements under the crossover. Eliminating the spatial filter entirely, while keeping the 62-km finite difference, had little effect, increasing the rms difference from 7 to 8 cm s^{-1} for the cross-track components of velocity. Retaining the 50-km filter while reducing the span of the finite difference had a much more drastic effect. Spans of 50, 37, 25, and 12.5 km, followed by the 50-km filter, resulted in rms differences of 8, 10, 13 and 15 cm s^{-1}, respectively, compared to 7 cm s^{-1} for the 62-km span.

An alternative to the use of finite difference operators is to fit linear regressions to a span of points. *Morrow et al.* [1994] used a 25-point linear regression for Geosat data, which removed most variability with scales less than 100 km. Given the lower noise level in TOPEX data, present calculations are being made with 12–20 point linear regres-

sions [*D. Chelton*, personal communication, 1996]. For the crossover considered here, use of a ten-point linear regression (to compare to the ten-point difference) results in rms differences of 9–11 cm s^{-1} between TOPEX and the spatially averaged 100-m cross-track components of velocity. This is larger than the 7–8 cm s^{-1} obtained using the 10-point finite difference, with or without the 50-km loess spatial filter, due to the decrease in the smoothing of the linear fit [*Schlax and Chelton*, 1992]. Use of a 12–16 point linear fit approximately reproduces the results using the ten-point difference and the 50-km loess spatial filter.

Our conclusion is that the 10-point finite difference operator, followed by the 50-km loess filter, is as reasonable a choice of gradient operator as any other simple option in this region of the ocean. A linear regression using 12–16 points would work as well. The appropriate scale of the gradient operator may differ in other regions. For global applications, more conservative spans of 16–20 points might be advised. Decreasing the scale of the operator below 50 km rapidly amplifies the noise in the calculation, requiring additional smoothing. There may be specific instances when it is worth pushing the spatial resolution to smaller scales, but only if the signal is strong enough to stand out above the increased noise.

Finally, how do these levels of velocity uncertainty relate to the expected levels of uncertainty in altimeter heights? As a first estimate we assume that errors in height are uncorrelated and propagate the error in height through the geostrophic calculation using the simple finite difference of 62 km (without a subsequent filter):

$$S_V{}^2 = 2S_H{}^2\left(\frac{\partial V}{\partial H}\right)^2 = 2S_H{}^2\left(\frac{g}{fL}\right)^2 \qquad \text{(A2)}$$

where L is the span of the finite difference. For normal values of g and f at midlatitudes and for $L = 62$ km, an uncertainty of 7.6 cm s^{-1} in cross-track velocity corresponds to an rms uncertainty in height of 3.3 cm. Uncertainties of 3–5 cm s^{-1} correspond to rms height uncertainties of approximately 2 cm. These uncertainties in height compare very well to previous estimates of 2.7–3.3 cm [*Katz et al.*, 1995] and 3.3–3.7 cm [*Picaut et al.*, 1995], from inverted echo sounders and from moorings in deep water on which strings of temperature and conductivity sensors allow calculation of continuous time series of dynamic height.

Acknowledgments. Support for PTS and CJ was provided by JPL grant 958128, ONR grant N0014-92-J-1631 and NASA grants NAGW-2475 and NAF-5-30553. Support for MDL was provided by JPL grant 958128. Support for TKC was provided by ONR grant 14-92-J-1584 and NSF grant OCE-9216411. Support for PPN was provided by ONR grant N0014-91-J-1016. The ONR support was part of the Eastern Boundary Current ARI (Code 322, Physical Oceanography). TOPEX data were provided by the Jet Propulsion Laboratory. Tidal corrections were provided by Gary Egbert and Andrew Bennett. The mooring design, deployment, and recovery were made possible by technical support from Oregon State University's Buoy Group, Scripps Institution of Oceanography's Instrument Development Group, Woods Hole Oceanographic Institution's Buoy Group, University of Miami's Buoy Group, and the captain and crew of the R/V *Point Sur*. Discussions with Dudley Chelton, Michael Kosro, Michael Freilich, and Kathie Kelly were useful during the analysis. Careful reviews by Fabrice Hernandez and two anonymous reviewers resulted in a clearer and more concise paper.

References

Brink, K.H., and T.J. Cowles, The coastal transition zone program, *J. Geophys. Res., 96*, 14,637-14,647, 1991.

Brink, K.H., R.C. Beardsley, P.P. Niiler, M. Abbott, A. Huyer, S. Ramp, T. Stanton, and D. Stuart, Statistical properties of near-surface flow in the California coastal transition zone, *J. Geophys. Res., 96*, 14693-14,706, 1991.

Callahan, P. S., TOPEX/POSEIDON Project GDR User's Handbood, *Publ. JPL D-8944*, rev. A., Jet Propul. Lab., Pasadena, Calif., 1993.

Chelton, D.B., M.G. Schlax, D.L. Witter, and J.G. Richman, Geosat altimeter observations of the surface circulation of the Southern Ocean, *J. Geophys. Res., 95*, 17,877-17,903, 1990.

Chereskin, T.K., Direct evidence for an Ekman balance in the California Current, *J. Geophys. Res., 100*, 18,261-18,271, 1995.

Chereskin, T. K., and A. J. Harding, Modeling the performance of an acoustic Doppler current profiler, *J. Atmos. Oceanic Technol., 10*, 41-63, 1993.

Chereskin T. K., E. Firing, and J. A. Gast, On identifying and screening filter skew and noise bias in acoustic Doppler current profiler measurements, *J. Atmos. Oceanic Technol., 6*, 1040-1054, 1989.

D'Asaro, E.A., C.C. Eriksen, M.D. Levine, P. Niiler, C.A. Paulson, and P. Van Meurs, Upper-Ocean inertial currents forced by a strong storm, I, Data and comparisons with linear theory, *J. Phys. Oceanogr., 25*, 2909-2936, 1995.

Egbert, G.D., A.F. Bennett, and M.G.G. Foreman, TOPEX- POSEIDON tides estimated using a global inverse model, *J. Geophys. Res., 99*, 24,821-24,852, 1994.

Fu, L.-L., E.J. Christensen, C.A. Yamarone Jr., M. Lefebvre, Y. Ménard, M. Dorrer, and P. Escudier, TOPEX/POSEIDON mission overview, *J. Geophys. Res., 99*, 24,369-24,382, 1994.

Huyer, A. P.M. Kosro, J. Fleischbein, S.R. Ramp, T. Stanton, L. Washburn, F.P. Chavez, T.J. Cowles, S.D. Pierce, and R.L. Smith, Currents and water masses of the coastal transition zone off northern California, June to August 1988, *J. Geophys. Res., 96*, 14,809-14,831, 1991.

Katz, E.J., A. Busalacchi, M. Bushnell, F. Gonzalez, L. Gourdeau, M. McPhaden, and J. Picaut, A comparison of coincidental time series of the ocean surface height by satellite altimeter, mooring, and inverted echo sounder, *J. Geophys. Res., 100*, 25,101-25,108, 1995.

Kosro, P.M., et al., The structure of the transition zone between coastal waters and the open ocean off northern California, winter and spring, 1987, *J. Geophys. Res., 96*, 14,707–14,731, 1991.

Menkes, C., J.-P. Boulanger, and A. J. Busalacchi, Evaluation of TOPEX and basin-wide Tropical Ocean and Global Atmosphere-Tropical Atmosphere Ocean sea surface topographies and derived geostrophic currents, *J. Geophys. Res., 100*, 25,087–25,099, 1995.

Mesias, J.M., and P.T. Strub, An inversion method to determine ocean surface currents using irregularly sampled altimetry data, *J. Atmos. Oceanic Technol., 12*, 830–849, 1995.

Morrow, R., R. Coleman, J. Church, and D. Chelton, Surface eddy momentum flux and velocity variances in the Southern Ocean from Geosat altimetry, *J. Phys. Oceanogr., 24*, 2050–2071, 1994.

Paduan, J.D., and P.P. Niiler, A Lagrangian description of motion in Northern California coastal transition filaments, *J. Geophys. Res., 95*, 18,095–18,109, 1990.

Picaut, J., A.J. Busalacchi, M.J. McPhaden, L. Gourdeau, F.I. Gonzalez, and E.C. Hackert, Open-ocean validation of TOPEX-POSEIDON sea level in the western equatorial Pacific, *J. Geophys. Res., 100*, 25,109–25,129, 1995.

Preisendorfer, R. W., *Principal Component Analysis in Meteorology and Oceanography*, 425 pp., Elsevier, New York, 1988.

Ramp, S.R., P.F. Jessen, K.H. Brink, P.P. Niiler, F.L. Daggett, and J.S. Best, The physical structure of cold filaments near

Point Arena, California, during June 1987, *J. Geophys. Res., 96,* 14,859-14,884, 1991.

Schlax, M.G., and D.B. Chelton, Frequency domain diagnostics for linears smoothers, *J. Am. Stat. Assoc., 87,* 1070-1081, 1992.

Stabeno, P.J., and R.L. Smith, Deep-sea currents off northern California, *J. Geophys. Res., 92,* 755-771, 1987.

Strub, P.T., P.M. Kosro, A. Huyer, and CTZ Collaborators, The nature of the cold filaments in the California Current System, *J. Geophys. Res., 96,* 14,743-14,768, 1991.

Walstad, L.J., J.S. Allen, P.M. Kosro, and A. Huyer, Dynamics of the coastal transition zone through data assimilation studies, *J. Geophys. Res., 96,* 14,959-14,979, 1991.

Wunsch, C., and D. Stammer, The global frequency-wavenumber spectrum of oceanic variability from TOPEX/POSEIDON altimetric measurements, *J. Geophys. Res., 100,* 24,895-24,910, 1995.

Yu, Y., W. J. Emery, and R. R. Leben, Satellite altimeter derived geostrophic currents in the western tropical Pacific during 1992-1993 and their validation with drifting buoy trajectories, *J. Geophys. Res., 100,* 25,069-25,085, 1995.

P. T. Strub, C. James, and M. D. Levine, College of Oceanic and Atmospheric Sciences, Oregon State University, 104 Ocean Administration Building, Corvallis, OR 97331-5503. (email: tstrub@oce.orst.edu; corinne@oce.orst.edu; mlevine@oce.orst.edu)

T. K. Chereskin and P. P. Niiler, Scripps Institution of Oceanography, 9500 Gilman Drive, La Jolla, CA 92093-0230. (email: tchereskin@ucsd.edu; pniiler@ucsd.edu)

(Received May 7, 1996; revised October 23, 1996;
accepted January 3, 1997.)